

Test-Time Adaptation for Anomaly Segmentation via Topology-Aware Optimal Transport Chaining

Ali Zia ^{*1} Usman Ali ^{*2} Umer Ramzan ² Abdul Rehman ² Abdelwahed Khamis ³ Wei Xiang ¹

Abstract

Deep topological data analysis (TDA) offers a principled framework for capturing structural invariants such as connectivity and cycles that persist across scales, making it a natural fit for anomaly segmentation (AS). Unlike threshold-based binarisation, which produces brittle masks under distribution shift, TDA allows anomalies to be characterised as disruptions to global structure rather than local fluctuations. We introduce TopoOT, a topology-aware optimal transport (OT) framework that integrates multi-filtration persistence diagrams (PDs) with test-time adaptation (TTA). Our key innovation is Optimal Transport Chaining, which sequentially aligns PDs across thresholds and filtrations, yielding geodesic stability scores that identify features consistently preserved across scales. These stability-aware pseudo-labels supervise a lightweight head trained online with OT-consistency and contrastive objectives, ensuring robust adaptation under domain shift. Across standard 2D and 3D anomaly detection benchmarks, TopoOT achieves state-of-the-art performance, outperforming the most competitive methods by up to +24.1% mean F1 on 2D datasets and +10.2% on 3D AS benchmarks.

1. Introduction

Test-time training (TTT) has emerged as a promising paradigm for adapting models under distribution shift, but most approaches remain limited to entropy minimisation or feature consistency, without structured reasoning about data geometry (Sun et al., 2020; Volpi et al., 2022; Zhang et al., 2022). A central limitation of many existing TTT

^{*}Equal contribution ¹School of Computing, Engineering & Mathematical Sciences, La Trobe University, Melbourne, Australia

²School of Engineering and Applied Sciences, GIFT University, Gujranwala 52250, Pakistan ³CSIRO, Australia. Correspondence to: Ali Zia <A.Zia@latrobe.edu.au>.

Preprint. January 29, 2026.

approaches, particularly in dense prediction tasks, is their reliance on heuristic pseudo-labels or confidence thresholds (Liang et al., 2025; Costanzino et al., 2024a; Zhang et al., 2025), which are non-robust (brittle) under distribution shift. Incorporating explicit structural priors provides a principled way to address this gap. The integration of TDA, which extracts persistent features such as connectivity and holes across scales (Zia et al., 2024), and OT, which provides a principled framework for aligning distributions (Cuturi, 2013; Peyré et al., 2019), has received little attention in this context. AS is a particularly compelling domain in which to explore this integration, because it requires pixel-level localisation of irregular patterns whose connectivity and shape are critical, yet conventional threshold-based binarisation often collapses under shift (Cao et al., 2024). By combining TDA’s ability to capture structural persistence with OT’s alignment capabilities, TTT can move beyond heuristics and yield more stable and adaptive anomaly delineation.

AS demands fine-grained identification of abnormal regions in test images, typically without access to anomalous training examples (Tao et al., 2022). Most existing methods generate continuous anomaly maps that must be binarised (Cao et al., 2024), but thresholds derived from nominal data are brittle across categories and anomaly types (Tong et al., 2024; Wu et al., 2024; Zhou et al., 2024a). Supervised approaches (Baitieva et al., 2024; Hu et al., 2024b; Zhu et al., 2024; Ding et al., 2022) can achieve strong performance but require extensive annotation, which is impractical for rare or heterogeneous anomalies (Xie & Mirmehdi, 2007; Qiu et al., 2019). Unsupervised methods (Guo et al., 2025; He et al., 2024; Ali et al., 2025) are trained only on nominal data, rely on static thresholds, and fail to preserve structural consistency under domain shift.

Beyond the reliance on brittle thresholds, current approaches to AS and TTA face several underexplored challenges. First, robustness under distribution shift remains insufficient, benchmarks such as MVTec-AD (Bergmann et al., 2019), VisA (Zou et al., 2022), and Real-IAD (Wang et al., 2024a) often underestimate the variability of anomalies, yet in practice, even minor domain shifts can cause embeddings or thresholds to fail catastrophically. Second, AS research has concentrated on 2D image settings, leaving structural guid-

ance in 3D anomaly detection and segmentation (AD&S) largely unaddressed (Li et al., 2024), despite its importance in industrial inspection. Third, pseudo-labels used in existing TTT frameworks are often derived from entropy or heuristic criteria, providing no guarantees of structural consistency across runs or domains (Zhao et al., 2024). Finally, while efficiency is critical for deployment, there has been little exploration of methods that simultaneously remove threshold dependence and remain lightweight enough for real-time adaptation.

These gaps underscore the need for a framework that (i) eliminates brittle thresholding, (ii) stabilises noisy structural descriptors, (iii) incorporates explicit priors into TTA, and (iv) extends naturally to 3D settings. We propose **TopoOT**, a framework that stabilises pseudo-labels using multi-scale topological cues via persistent homology and aligns them with OT, providing structure-aware supervision for TTT.

Although our experiments focus on AS, we view this task as the most natural and demanding testbed for a first exploration of structurally guided TTT, since anomalies disrupt connectivity, boundaries, and higher-order organisation, precisely the features that TDA and OT are designed to capture. Establishing effectiveness in this setting provides a foundation for broader machine learning tasks where structural stability is critical, including domain adaptation under distribution shift (Dan et al., 2024), weak-signal detection in scientific data, and fine-grained visual analysis (Michaeli & Fried, 2024), where subtle structural cues determine class boundaries (Zia et al., 2024).

TopoOT embeds structural alignment into the TTT framework. The key contributions are:

- To overcome threshold brittleness, we introduce an **OT-guided, structure-aware representation** that integrates multi-scale topological cues from PDs. This representation produces pseudo-labels that provide adaptive and data-driven supervision for TTT.
- To stabilise noisy topological descriptors, we propose a novel **OT chaining** mechanism that aligns PDs both within a filtration (*cross-PD*) and across sub- and super-level filtrations (*cross-level*), retaining only consistently transported features and discarding spurious ones.
- To integrate structural priors into TTT, we design a lightweight head trained online with two complementary objectives: **OT-consistency**, which preserves *transport-aligned structures*, and *contrastive separation*, which sharpens anomalous versus nominal boundaries.
- Our approach is *plug-and-play*, integrating seamlessly with different backbones and extending natu-

rally across modalities, generalising from 2D to 3D AD&S (point clouds and multimodal anomaly detection), where connectivity and shape priors are especially critical.

Across diverse datasets, our design consistently delivers robust and generalisable AS. Evaluated on **5** 2D/3D benchmarks and **7** backbones, TopoOT achieves F1 gains up to **+24.1%** on 2D and **+10.2%** on 3D compared to the existing SOTA. It further generalises across models and domains, surpassing TTT baselines by up to **+4.8%**. The lightweight TTT module of TopoOT remains highly efficient, running at **121** FPS while using only **349** MB of GPU memory.

2. Related Work

Anomaly Detection and Segmentation: AS under distribution shift is challenging as it requires fine-grained detection without supervision, structural priors that capture meaningful data characteristics, and adaptation to unseen test-time distributions. Unsupervised AD&S avoids labelled anomalies by learning from nominal data (He et al., 2024). Early reconstruction-based methods used autoencoders (Fang et al., 2023; Park et al., 2024; Zuo et al., 2024; Zhou et al., 2024b; Wang et al., 2024b), inpainting (Li et al., 2020; Nakanishi et al., 2022; Zavrtanik et al., 2021a; Pirnay & Chai, 2022; Luo et al., 2024), or diffusion models (Yao et al., 2024a; Fučka et al., 2024; Jiang et al., 2024), but often produced blurry reconstructions or overfit to normal patterns. Feature-based approaches compare embeddings to nominal references (Park et al., 2024; Roth et al., 2022; Defard et al., 2021), or use teacher–student frameworks (Deng & Li, 2024; Rudolph et al., 2023; Zhang et al., 2023; Gu et al., 2024) for inductive bias. Generative priors via normalizing flows (Yao et al., 2024b; Gudovskiy et al., 2022; Lei et al., 2023; Kim et al., 2023) or synthetic anomalies (Aota et al., 2023; Li et al., 2024; Hu et al., 2024a; Chen et al., 2024) improved detection, yet typically lack pixel-level precision. Methods such as PatchCore (Roth et al., 2022) and PaDiM (Defard et al., 2021) leverage pre-trained backbones, but remain threshold-dependent and structurally agnostic.

Optimal Transport in Vision: OT has been widely applied in computer vision for distribution alignment (Peyré et al., 2019; Cuturi, 2013; Bonneel & Digne, 2023), including domain adaptation (Ge et al., 2021; Fan et al., 2024; Luo & Ren, 2023), object detection, and image restoration (Adrai et al., 2023). In anomaly detection, (Liao et al., 2025) employed robust Sinkhorn distances for industrial inspection. These works show OT’s adaptability for handling domain discrepancies, but they typically operate at the distribution level and do not exploit OT for structured feature selection or test-time supervision. While our approach employs a novel *OT chaining* mechanism, entropically regularised OT helps

align PDs through cross-PD filtration to capture feature evolution and cross-level filtration to integrate complementary structures, thereby preserving consistently transported features and discarding spurious ones.

Topological Priors and Test-Time Training: TDA, particularly persistent homology (PH), has been applied in medical imaging to capture shape and multi-scale structure (Adcock et al., 2014; Berry et al., 2020; Crawford et al., 2020; Garside et al., 2019; Kanari et al., 2018). Yet most uses are offline and not integrated into adaptive learning (Zia et al., 2024). TTT (Liang et al., 2025; Nado et al., 2020; Kim et al., 2022; Colomer et al., 2023; Nguyen et al., 2023; Khurana et al., 2021) adapts models on-the-fly with self-supervised objectives, and TTT4AS (Costanzino et al., 2024a) extended this idea to AS with heuristic pseudo-labels. However, these lack explicit structural reasoning and remain sensitive to noise.

Our approach combines PH-based filtrations with OT alignment to derive stable pseudo-labels, which then guide a lightweight TTT head. This integration moves beyond heuristic thresholds by embedding structural priors directly into TTA, yielding robust and topologically consistent AS.

3. OT-Guided Test Time Structural Alignment Framework

Problem Formulation: Conventional AS methods produce a dense anomaly score map and obtain binary masks through thresholds calibrated on nominal validation data (Costanzino et al., 2024a) (e.g., percentile rules). Such thresholds are dataset-specific, fail under distribution shift, and often generate masks that under-cover or over-extend the anomalous region. Moreover, they operate pixel-wise and neglect structural information in the anomaly map. To address these limitations, we represent anomaly maps as PDs, which capture multi-scale topological features such as connected components and holes. Figure 1 provides an overview of our proposed TopoOT framework. We then introduce an OT-based scoring scheme that evaluates PDs across filtrations and levels, ranking components by their cross-scale consistency. This formulation replaces fixed thresholding with a structural scoring approach designed to produce consistent anomaly masks under distribution shift.

Building on this, PDs derived from sub- and super-level filtrations provide the candidate anomaly structures. We apply OT alignment across filtration levels to retain components that persist with low transport cost, while discarding unstable features (that don’t persist across PDs). The ranked components are then back-projected into the image domain to form pseudo-labels, which serve as data-dependent supervision at inference in place of fixed thresholds.

During TTT, we keep the replaceable backbone frozen and

update only a lightweight head. This head is optimised with two complementary objectives: (i) OT-consistency, which encourages predictions to remain aligned with the stable structures identified by OT, and (ii) contrastive separation, which increases the margin between anomalous and nominal regions. The combination of these objectives yields a segmentation mask that is guided by OT-derived pseudo-labels rather than fixed thresholds.

3.1. Multi-scale Filtering as Feature Generation

We start from a continuous anomaly map $A : \Omega \rightarrow [0, 1]$ defined over the pixel lattice Ω , same as (Costanzino et al., 2024a). To capture structural variation at multiple thresholds, we fix a sequence of increasing thresholds $\mathcal{T} = \{\tau_1 < \tau_2 < \dots < \tau_N\}$. For each $\tau_k \in \mathcal{T}$, we define the sublevel and superlevel sets $S_{\tau_k}^{\text{sub}} = \{p \in \Omega : A(p) \leq \tau_k\}$, and $S_{\tau_k}^{\text{sup}} = \{p \in \Omega : A(p) \geq \tau_k\}$. These subsets naturally induce cubical complexes $K_{\tau_k}^{\text{sub}}$, $K_{\tau_k}^{\text{sup}}$, where each cell corresponds to a contiguous block of pixels (a cube in the grid) included whenever its vertices satisfy the relevant threshold condition. The “cubical” construction is appropriate for images/grids, because it respects the pixel adjacency and can be computed efficiently.

By varying the thresholds τ_k , we obtain nested sequences (filtrations) of level sets: $K_{\tau_1}^f \subset K_{\tau_2}^f \subset \dots \subset K_{\tau_N}^f$, $f \in \{\text{sub, sup}\}$, where we assume $\tau_1 < \dots < \tau_N$ for sublevel sets and $\tau_1 > \dots > \tau_N$ for superlevel sets. From these filtrations, we compute persistent homology in dimensions $h \in \{0, 1\}$. The result is a persistence diagram \mathcal{P}_f^h at each threshold level.

For a filtration $\{K_{\tau_k}^f\}_{k=1}^N$, persistent homology computes, for each dimension h , the sequence of homology groups $H_h(K_{\tau_1}^f), \dots, H_h(K_{\tau_N}^f)$, where $H_h(K_{\tau_k}^f)$ denotes the h -th homology group of the complex $K_{\tau_k}^f$. This tracks how h -dimensional topological features (connected components for $h = 0$, loops for $h = 1$) appear and disappear along the sequence. A feature c is born at the smallest index k such that it appears in $H_h(K_{\tau_k}^f)$, and dies at the first index $\ell > k$ where it merges into an older feature or becomes trivial. The pair $(b_c, d_c) = (\tau_k, \tau_\ell)$ encodes its lifetime (persistence), and the persistence diagram $\mathcal{P}_f^h = \{(b_c, d_c) \mid c \text{ is an } h\text{-dimensional feature in the filtration}\}$ is the multiset of all such birth-death pairs. For a given threshold τ_k , the diagram $\mathcal{P}_f^h[\tau_k]$, the H_0 (homology in dimension 0) captures connected components that are how new components appear (birth) and merge (death) across thresholds. H_1 (1-dimensional homology) captures loops or holes (voids), features that appear in superlevel or sublevel sets and disappear at some higher (or lower) threshold. Background on cubical complexes in Appendix A.8.

Each topological feature c in a diagram is represented as a pair (b_c, d_c) of birth and death times; its persistence

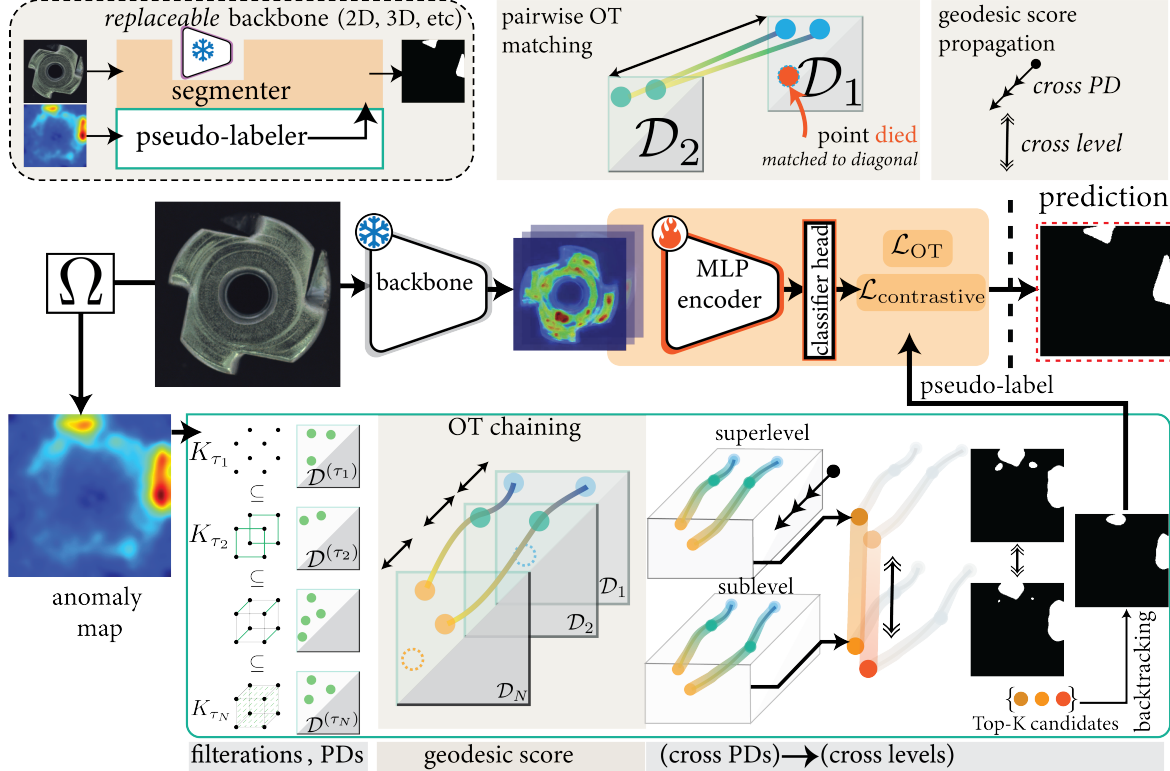


Figure 1. TopoOT Test-time Training for Anomaly Segmentation. (Top Left) pipeline simplified view. (Bottom) detailed view. TopoOT replaces conventional thresholding by stabilising anomaly evidence via cross-PD OT matching within each filtration, then fusing sub- and super-level scores with cross-level OT. The resulting global scores yield Top-K pseudo-labels that supervise a lightweight head for final segmentation.

$\text{pers}(c) = d_c - b_c$ reflects how long it persists. Features with large persistence are more likely to correspond to “meaningful” structural anomalies, while those close to the diagonal (small persistence) are often noise. These ideas align with the discussion review paper by (Zia et al., 2024), which emphasises that PDs and barcodes are robust summaries of topological features of data across scales, invariant to small perturbations, deformation, and noise. The outputs $\{\mathcal{P}_{\text{sub}}^h[\tau_k]\}_{k=1}^N$, and $\{\mathcal{P}_{\text{sup}}^h[\tau_k]\}_{k=1}^N$ serve as multi-scale candidate features. They form the input to the OT-based alignment steps. Rather than acting as direct decision thresholds, these persistence diagrams are treated as a rich feature generation mechanism, capturing anomalies’ connected components and holes over multiple scales, which allows the downstream optimal transport stage to judge stability and discriminability among structural candidates.

3.2. Geodesic Scoring of Topological Features

The PDs derived from sub- and super-level filtrations provide a rich but noisy set of candidate features. Many short-lived components arise due to local perturbations in the anomaly map, which, if treated directly, would degrade the reliability of pseudo-labels. A key challenge is how to aggregate these diverse features into a concise set of components that can be meaningfully traced back to the original image. A possible solution is computing a barycenter of diagrams (Turner et al., 2014), but barycenters discard the natural order of filtrations and blur fine-scale structures. Mapping diagrams into kernels or persistence images (Reininghaus et al., 2015) is another alternative, but these yield global embeddings without interpretable correspondences. In contrast, we propose aggregating information by following the flow of diagrams within each filtration sequence using Optimal Transport Chaining. This approach consolidates features into stable representatives for both the sublevel and superlevel filtrations independently, and then fuses the two levels to obtain consensus features.

Formally, let $P = \{p_i = (b_i, d_i)\}_{i=1}^m$ and $Q = \{q_j = (b'_j, d'_j)\}_{j=1}^n$ be two persistence diagrams, used here as shorthand for $\{\mathcal{P}_f^h[\tau_k]\}$ at different thresholds or filtrations. We define the ground cost as the squared Euclidean distance between pairs of features, and compute the entropic OT plan:

$$\Pi^* = \arg \min_{\Pi \in \mathcal{U}(P, Q)} \langle C, \Pi \rangle + \varepsilon H(\Pi) \quad (1)$$

where $\mathcal{U}(P, Q)$ denotes the set of admissible couplings between P and Q , and $H(\Pi)$ is the entropy of the transport plan. The regularisation parameter $\varepsilon > 0$ ensures numerical stability and smooth alignments. In our framework, all transport plans are therefore entropy-regularised Sinkhorn solutions rather than exact Wasserstein couplings because they yield smooth, differentiable, and numerically stable alignments; see Appendix A.6 for further details.

We exploit this transport plan through a novel **OT chaining** mechanism, which consists of two complementary modes: *cross-PD* (intra) filtration and *cross-level* (inter) filtration alignment. In *cross-PD* filtration alignment, OT is applied within a single filtration (sublevel or superlevel) between persistence diagrams at different thresholds τ_k and τ_ℓ . This process identifies features that persist consistently through the filtration, and each candidate c receives a stability score:

$$s(c) = \max_j \frac{\Pi^*(i(c), j)}{1 + \sqrt{C(i(c), j)}} \cdot \alpha \text{pers}(c) \quad (2)$$

where Π^* is the entropic OT plan between diagrams, $C(i(c), j)$ is the ground cost, $i(c)$ denotes the index of the birth–death pair representing feature c in its persistence diagram, and $\text{pers}(c)$ is the persistence of c as defined in Sec. 3.1. Since C is defined as squared Euclidean distances, we use \sqrt{C} in the denominator to restore a linear distance scale, ensuring that score decay is proportional to distance rather than quadratic. This softens penalisation and allows moderately stable matches to contribute, instead of filtering too aggressively. The maximisation is taken over all possible partners j of candidate c within the filtration, where j indexes features in the comparison persistence diagram. In this way, $s(c)$ reflects the strongest OT-stable match. When points don’t get matched between PDs, they are coupled to the diagonal as in standard TDA practice (see Sec. 3.1 and Appendix A.7), ensuring that chain stability scores naturally account for vanishing features. The factor $\alpha \geq 0$ controls the influence of persistence on ranking. Top- M components are selected by maximising stability and persistence and minimising transport cost.

In *cross-level* filtration alignment, we compare candidate sets from the sublevel and superlevel filtrations. Applying OT across sublevel and superlevel filtrations integrates complementary topological cues. Sublevel filtrations emphasise how connected components emerge and merge, while superlevel filtrations highlight how voids and holes evolve. By aligning these perspectives, the method retains structural features that are consistently expressed across both, thereby suppressing spurious components and strengthening anomaly cues. Each candidate c is evaluated with the same stability score $s(c)$ defined above, but here the partner set is drawn from the opposite filtration. This ensures that features are retained only if they exhibit both cross-PD scale

persistence and cross-level filtration consistency. The top- K ranked candidates across both filtrations are then collected to form the final set \mathcal{C}^* .

The surviving candidates in \mathcal{C}^* are projected back to their pixel-level supports on the anomaly map, yielding *OT-guided pseudo-labels* \tilde{Y}_{OT} . These pseudo-labels are inherently multi-scale and data-adaptive, as they emerge from stable OT couplings rather than fixed thresholds. These retained features correspond to connected regions or holes, e.g., defects or gaps, that persist across the filtration process and reflect semantically meaningful structures in the input space. By filtering out noise-induced artefacts, OT alignment produces pseudo-labels that provide robust supervision for TTT.

The surviving candidates in \mathcal{C}^* are then projected back to their pixel-level supports on the anomaly map, yielding OT-guided pseudo-labels \tilde{Y}_{OT} . This backprojection is possible because the filtrations in Sec. 3.1 are built by thresholding the anomaly map $A : \Omega \rightarrow [0, 1]$ at different anomaly score levels. As these thresholds vary, each retained feature $c \in \mathcal{C}^*$ corresponds to a connected component or hole that remains present in the thresholded maps for all levels between its birth and death (b_c, d_c) . Thus b_c and d_c can be interpreted directly as anomaly-score levels at which that structure appears and disappears in the original image. To obtain a pixel-level support for c , we choose a representative level near its death time and mark all pixels whose anomaly score exceeds this level. Formally, for each $c \in \mathcal{C}^*$ we define the backprojection threshold as $\tau_{\text{bp}}(c) = d_c$, and the pixel-level support of c as the superlevel set

$$\Gamma(c) = \{p \in \Omega : A(p) \geq \tau_{\text{bp}}(c)\}. \quad (3)$$

Aggregating the Top- K retained candidates, the OT-guided pseudo-label mask is defined as

$$\tilde{Y}_{\text{OT}}(p) = \mathbf{1}(\exists c \in \mathcal{C}^* \text{ such that } p \in \Gamma(c)), \quad p \in \Omega, \quad (4)$$

which corresponds to the union of the pixel-level supports of the OT-stable features.

For added robustness, one can be a bit conservative when setting the threshold to ensure that the back projected region remains safely within the range where the feature is still present in the filtration. This can be achieved by introducing a small offset $\delta_{f(c)}$ and thresholding at $\{p : A(p) \geq \max\{0, d_c - \delta_{f(c)}\}\}$, where $f(c) \in \{\text{sublevel, superlevel}\}$ denotes the filtration type. In practice, $\delta_{f(c)}$ is chosen as a small, fixed fraction of the $[0, 1]$ anomaly-score range (e.g., 0.2) and kept constant across all datasets. . These pseudo-labels are inherently multi-scale and data-adaptive, as they emerge from stable OT couplings rather than fixed thresholds. These retained features correspond to connected regions or holes, e.g., defects or gaps, that persist across the filtration process and reflect semantically meaningful

structures in the input space. By filtering out noise-induced artefacts, OT alignment produces pseudo-labels that provide robust supervision for TTT.

3.3. TopoOT Test-Time Training

The final stage of our pipeline leverages the OT-guided pseudo-labels \tilde{Y}_{OT} to adapt the model during inference. Since the backbone feature extractor is frozen, adaptation is performed through a lightweight segmentation head h_{ψ} attached to the anomaly map representation. This design ensures that the adaptation cost at test time remains negligible, while still allowing the predictions to be tailored to the distribution of the current sample. Training h_{ψ} is guided by two complementary objectives. First, we introduce an **OT-consistency** loss that encourages the segmentation head h_{ψ} to reproduce the spatial structures encoded in \tilde{Y}_{OT} . Given the deviations from the OT-aligned pseudo-labels $\mathcal{L}_{\text{OT}} = \|\hat{Y} - \tilde{Y}_{\text{OT}}\|_2$ which enforces consistency with stable transport couplings and prevents overfitting. Second, we incorporate a margin-based contrastive objective to sharpen local decision boundaries in the embedding space produced by h_{ψ} . From the OT-derived pseudo-labels $\tilde{Y}_{\text{OT}} \in \{0, 1\}^{H \times W}$, we sample pixel pairs (p, q) as similar when $\tilde{Y}_{\text{OT}}(p) = \tilde{Y}_{\text{OT}}(q)$ and dissimilar otherwise. Let $z_p, z_q \in \mathbb{R}^D$ denote the L2-normalised embeddings of those pixels. The contrastive loss is:

$$\begin{aligned} \mathcal{L}_{\text{contrastive}} = & (1 - y_{pq}) \|z_p - z_q\|_2^2 \\ & + y_{pq} \left[\max(0, m - \|z_p - z_q\|_2) \right]^2 \end{aligned} \quad (5)$$

where $y_{pq} \in \{0, 1\}$ encodes dissimilarity and $m > 0$ is a margin. This loss compacts same-label embeddings while enforcing a minimum separation between background and anomalous regions, improving robustness to noise in \tilde{Y}_{OT} .

The combined loss is $\mathcal{L}_{\text{TTT}} = \mathcal{L}_{\text{OT}} + \lambda \mathcal{L}_{\text{contrastive}}$ with λ controlling the balance between structural consistency and contrastive separation. By optimising \mathcal{L}_{TTT} on each test sample, the segmentation head h_{ψ} adapts to dataset-specific distributions without requiring external supervision. The final segmentation mask \hat{Y}^{bin} is obtained through a canonical decision rule applied to the adapted predictions of h_{ψ} . Because h_{ψ} is trained on OT-guided pseudo-labels, this rule is adaptive to each test instance, avoiding dataset-specific calibration and eliminating heuristic threshold tuning.

This *test-time regularisation* departs from conventional schemes in two ways: (i) it grounds the adaptation signal in OT-aligned structures, stable across multi-scale filtrations, rather than raw anomaly scores; (ii) by integrating contrastive separation, it sharpens class boundaries instead of collapsing toward trivial solutions.

4. Experimental Setup

Datasets, Backbones, and Evaluation Protocol: We evaluate across both 2D and 3D anomaly detection benchmarks. For 2D, RGB datasets **MVTec AD** (Bergmann et al., 2019), **VisA** (Zou et al., 2022), and **Real-IAD** (Wang et al., 2024a) are used with backbones **PatchCore** (Roth et al., 2022), **PaDiM** (Defard et al., 2021), **Dinomaly** (Guo et al., 2025), and **MambaAD** (He et al., 2024). For 3D, we consider multimodal **MVTec 3D-AD** (RGB + point-cloud) (Bergmann et al., 2021b) and pure point-cloud **Anomaly-ShapeNet** (Li et al., 2024), using backbones **CMM** (Costanzino et al., 2024b), **M3DM** (Wang et al., 2023), and **PO3AD** (Ye et al., 2025).

While we report standard anomaly-detection metrics such as image-level AUROC (**I-AUROC**), pixel-level AUROC (**P-AUROC**), and pixel-level AUPRO (**P-AUPRO**) for completeness, our evaluation focuses on pixel-level **Precision**, **Recall**, **F1**, and **IoU** of the final binary masks. AUROC and AUPRO mainly assess ranking quality and can remain high despite poor mask quality under severe pixel imbalance (Bergmann et al., 2019; Zavrtanik et al., 2021b). In contrast, Precision, Recall, and F1 capture the accuracy of detected defect regions, balancing missed detections and false alarms, while IoU offers a stringent measure of spatial overlap (Costanzino et al., 2024a). These metrics align more closely with industrial inspection needs, where the fidelity of the delivered mask is the decisive criterion (Bergmann et al., 2021a).

Across both domains, we compare all methods against the TTT baseline **TTT4AS** (Costanzino et al., 2024a). Following **TTT4AS**, we binarise each backbone’s AS map at the statistical threshold $(\mu + c\sigma)$ and report this variant (**THR**) alongside the **TTT4AS** baseline. All experiments have been conducted on an NVIDIA RTX 5090 GPU with 32GB of VRAM. Detailed hyperparameters and architectural settings are provided in Appendix A.1. The lightweight TTT module of TopoOT runs at 121 FPS using 349 MB GPU memory for 2D inference; 3D inference has comparable memory use but lower FPS due to point-cloud operations. Per-dataset timing and memory profiles are given in Appendix A.2.

5. Results and Discussion

We validate TopoOT through analyses: (i) **2D and 3D AD&S**, benchmarking against state-of-the-art methods; (ii) **Cross Model Domain Adaptation**, where frozen feature extractors are paired with distinct anomaly score maps across 2D and 3D datasets; and (iii) **Ablation Studies**, assessing the contribution of each component. For detailed discussion of limitations and directions for future development, including efficiency tradeoffs and backbone dependency, refer to Appendix A.3.

5.1. 2D/3D AD&S

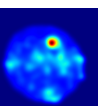
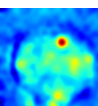
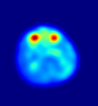
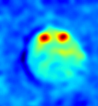
We present a comprehensive evaluation of **TopoOT** across five diverse datasets and seven state-of-the-art backbones. The I-AUROCP, P-AUROC, and P-AUPRO metrics are computed directly from each backbone’s AS map, while our method operates on the resulting anomaly maps to produce final binary segmentations. The results in Table 1 demonstrate superiority, with **TopoOT** consistently outperforming all baselines. The metrics are the mean per class within each dataset. Our method achieves a **+38.6%** F1 gain over **THR** and **+14.0%** over **TTT4AS** (Costanzino et al., 2024a) on MVTec AD (**PatchCore** (Roth et al., 2022)). For **PaDiM**, it surpasses **THR** by **+20.5%** and **TT4AS** by **+24.1%**. On VisA, it surpasses **TTT4AS** by **+19.7%** (**Dinomaly** (Guo et al., 2025)) and **+8.5%** (**MambaAD** (He et al., 2024)). For Real-IAD, **TopoOT** shows a **+12.3%** and **+11.8%** F1 improvement over **THR**, and a **+21.3%** and **+20.9%** gain over **TTT4AS** for the **Dinomaly** and **MambaAD** backbones, respectively. The advantage extends to 3D, with gains of

+20.7% (**CMM** (Costanzino et al., 2024b)) and **+24.5%** (**M3DM** (Wang et al., 2023)) over **THR** on MVTec 3D-AD, alongside **+10.2%** and **+2.2%** improvements over **TTT4AS**. On AnomalyShapeNet (**PO3AD** (Ye et al., 2025)), **TopoOT** also leads with a **+2.9%** and **+1.9%** F1 advantage.

Figure 2 shows that **TopoOT** yields sharper, more semantically coherent segmentations than competing methods. **TopoOT** secures concurrent gains in precision and recall, which in turn increase **IoU**, resulting in consistently superior segmentations across every benchmark. *Per-class quantitative and qualitative results* for each dataset are presented in the Appendix A.4 & A.5. **TopoOT** consistently achieves sharper boundaries and higher recall across categories. Even in challenging cases like thin or fragmented defects, it remains robust, clearly outperforming other methods across both 2D and 3D domains.

We also report a brief qualitative check on texture-heavy categories in Appendix A.10, where OT-based stability filtering reduces fragmentation and suppresses spurious islands,

Table 1. Comparison of binary segmentation results. Best results in **bold**; second-best in **blue**.

| Dataset | Backbone | I-AUROC | P-AUROC | P-AUPRO | TTT Method | Prec. | Rec. | F1 | IoU |
|---|---|---|---|---|---|---|---|--|---|
| MVTec AD (Bergmann et al., 2019) | PatchCore (Roth et al., 2022) | 0.991 | 0.981 | 0.934 | THR (Roth et al., 2022) | 0.351 | 0.507 | 0.136 | 0.299 |
| | PaDiM (Defard et al., 2021) | 0.979 | 0.975 | 0.921 | TTT4AS (Costanzino et al., 2024a) | 0.388 | 0.648 | 0.382 | 0.293 |
| VisA (Zou et al., 2022) | Dinomaly (Guo et al., 2025) | 0.987 | 0.987 | 0.945 | TopoOT | 0.550 | 0.720 | 0.522 | 0.387 |
| | MambaAD (He et al., 2024) | 0.943 | 0.985 | 0.910 | THR (Roth et al., 2022) | 0.452 | 0.507 | 0.354 | 0.317 |
| Real IAD (Wang et al., 2024a) | Dinomaly (Guo et al., 2025) | 0.893 | 0.989 | 0.939 | TTT4AS (Costanzino et al., 2024a) | 0.223 | 0.579 | 0.318 | 0.274 |
| | MambaAD (He et al., 2024) | 0.863 | 0.985 | 0.905 | TopoOT | 0.470 | 0.788 | 0.559 | 0.402 |
| MVTec 3D-AD (Bergmann et al., 2021b) | CMM (Costanzino et al., 2024b) | 0.954 | 0.993 | 0.971 | THR (Costanzino et al., 2024b) | 0.199 | 0.902 | 0.275 | 0.232 |
| | M3DM (Wang et al., 2023) | 0.945 | 0.992 | 0.964 | TTT4AS (Costanzino et al., 2024a) | 0.303 | 0.800 | 0.380 | 0.077 |
| AnomalyShapeNet (Li et al., 2024) | PO3AD (Ye et al., 2025) | 0.839 | 0.898 | 0.821 | TopoOT | 0.427 | 0.845 | 0.482 | 0.343 |
| Cookie | RGB | PC | GT | CMM-AS | THR | TTT4AS | TopoOT | M3DM-AS | THR |
| |  |  |  |  |  |  |  |  |  |
| Peach |  |  |  |  |  |  |  |  |  |

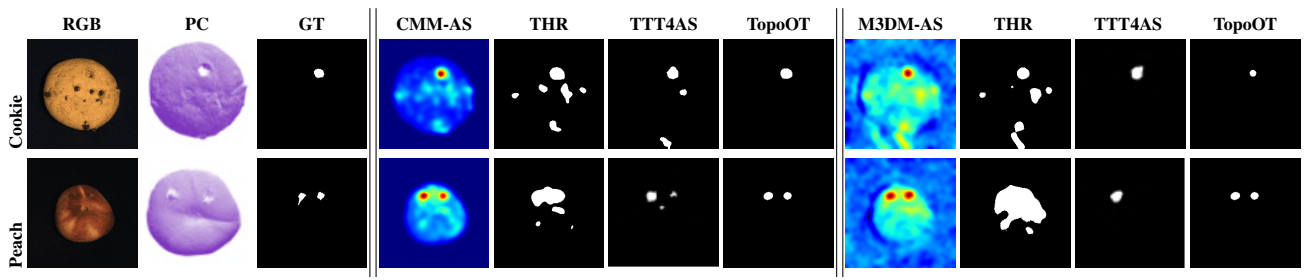


Figure 2. Qualitative comparison of AD&S methods for different objects using the MVTec 3D-AD dataset.

Table 2. Cross-model domain adaptation (features \rightarrow anomaly scores).

| Modality | Dataset | Source \rightarrow Target | Prec. | Rec. | F1 |
|----------|------------|---|-------|-------|-------|
| | | (Features \rightarrow Anomaly Scores) | | | |
| 2D | MVTec | PatchCore \rightarrow PaDiM | 0.419 | 0.673 | 0.430 |
| | | MambaAD \rightarrow Dinomaly | 0.459 | 0.712 | 0.502 |
| | | PatchCore \rightarrow MambaAD | 0.434 | 0.750 | 0.512 |
| 3D | MVTec-3DAD | CMM \rightarrow M3DM | 0.471 | 0.746 | 0.479 |
| | | M3DM \rightarrow CMM | 0.409 | 0.791 | 0.469 |

although performance remains bounded by the quality of the backbone anomaly map.

5.2. Cross Model Domain Adaptation

We validate a plug-and-play transfer strategy that pairs frozen *source* feature extractors with distinct *target* scoring heads across 2D (MVTec, VisA, Real-IAD) and 3D (MVTec-3DAD) domains. As shown in Table 2, the cross-model pipelines preserve topological structure and deliver practical quality without retraining. In 2D, transfers reach F1 up to **0.512** on Real-IAD (PatchCore \rightarrow MambaAD) and **0.502** on VisA (MambaAD \rightarrow Dinomaly), with recalls in the **0.71–0.75** band; in 3D, CMM \rightarrow M3DM offers the highest precision (**0.471**, F1 **0.479**), while M3DM \rightarrow CMM provides broad coverage (recall **0.791**). Importantly, these domain-adaptation results outperform established baselines across the evaluated datasets, confirming effective cross-model composition and providing a strong substrate for TopoOT to further consolidate gains via stability-aware OT pseudo-labels and adaptive boundary refinement for AS.

5.3. Ablation Studies

We validate TopoOT (Table 3). Individual cross-PD filtration alignments yield modest gains. The cross-level filtration alignment is key, providing a larger boost by integrating cross-scale information. The losses \mathcal{L}_{OT} and $\mathcal{L}_{contrastive}$ are effective together, enforcing prediction consistency and feature separation, respectively. Our complete model achieves top performance: **0.522** F1 on PatchCore, **0.482** on CMM, and **0.490** on M3DM.

We also examine the effect of retaining the Top- K OT-ranked components when projecting persistent features back to pixel space. Across all backbones and datasets, retaining only the most stable component ($K = 1$) consistently yields the best overall trade-off. While increasing K can slightly improve recall by covering additional candidate regions, it typically reduces precision because lower-ranked components are often small, noisy, or fragmented. Detailed quantitative results and per-setting breakdowns are provided in Appendix A.9.

6. Conclusion

We presented TopoOT, a topology-aware OT framework for anomaly segmentation that replaces brittle thresholding with OT-guided pseudo-labels and stabilises multi-scale persistence features through cross-PD and cross-level filtration chaining. A lightweight head trained with OT-consistency and contrastive objectives enables per-instance TTA that preserves structural stability while sharpening anomaly boundaries. TopoOT achieves SOTA performance on five standard benchmarks, and our theoretical analysis establishes stability and generalisation guarantees.

Despite these gains, TopoOT remains bounded by the quality of the underlying backbone anomaly maps motivating further efficiency improvements and tighter integration with representation learning. Future directions include accelerating persistence computation, extending the framework to spatiotemporal settings, and developing stronger unsupervised objectives that improve robustness under challenging textures and severe distribution shifts.

Table 3. Ablation study showing that combining all OT alignments with losses yields the highest performance.

| TopoOT Components | | | | | 2D-PatchCore | | | 3D-CMM | | | 3D-M3DM | | |
|-------------------------|---------------------------|----------------------------------|--------------------|-----------------------------|--------------|--------------|--------------|--------------|--------------|--------------|--------------|--------------|--------------|
| cross-PD _{Sub} | cross-PD _{Super} | cross-level _{Sub-super} | \mathcal{L}_{OT} | $\mathcal{L}_{contrastive}$ | Prec. | Rec. | F1 | Prec. | Rec. | F1 | Prec. | Rec. | F1 |
| ✓ | | | ✓ | | 0.440 | 0.310 | 0.365 | 0.410 | 0.455 | 0.382 | 0.290 | 0.730 | 0.390 |
| ✓ | | | | ✓ | 0.490 | 0.540 | 0.475 | 0.426 | 0.485 | 0.415 | 0.310 | 0.740 | 0.405 |
| | ✓ | | ✓ | | 0.375 | 0.620 | 0.390 | 0.085 | 0.820 | 0.118 | 0.280 | 0.755 | 0.380 |
| | ✓ | | | ✓ | 0.395 | 0.605 | 0.408 | 0.095 | 0.830 | 0.132 | 0.300 | 0.760 | 0.392 |
| ✓ | ✓ | ✓ | ✓ | | 0.520 | 0.690 | 0.510 | 0.420 | 0.800 | 0.470 | 0.500 | 0.750 | 0.485 |
| ✓ | ✓ | ✓ | | ✓ | 0.510 | 0.680 | 0.505 | 0.405 | 0.770 | 0.460 | 0.490 | 0.740 | 0.475 |
| ✓ | ✓ | ✓ | ✓ | ✓ | 0.550 | 0.720 | 0.522 | 0.427 | 0.845 | 0.482 | 0.564 | 0.767 | 0.490 |

References

Adcock, A., Rubin, D., and Carlsson, G. Classification of hepatic lesions using the matching metric. *Computer vision and image understanding*, 121:36–42, 2014.

Adrai, T., Ohayon, G., Elad, M., and Michaeli, T. Deep optimal transport: A practical algorithm for photo-realistic image restoration. *Advances in Neural Information Processing Systems*, 36:61777–61791, 2023.

Ali, U., Zia, A., Rehman, A., Ramzan, U., Hassan, Z., Sattar, T., Wang, J., and Xiang, W. 2d-3d feature fusion via cross-modal latent synthesis and attention-guided restoration for industrial anomaly detection. In *2025 International Conference on Digital Image Computing: Techniques and Applications (DICTA)*, pp. 1–8, 2025. doi: 10.1109/DICTA68720.2025.11302453.

Aota, T., Tong, L. T. T., and Okatani, T. Zero-shot versus many-shot: Unsupervised texture anomaly detection. In *Proceedings of the IEEE/CVF Winter Conference on Applications of Computer Vision*, pp. 5564–5572, 2023.

Baitieva, A., Hurich, D., Besnier, V., and Bernard, O. Supervised anomaly detection for complex industrial images. In *Proceedings of the IEEE/CVF Conference on Computer Vision and Pattern Recognition*, pp. 17754–17762, 2024.

Bergmann, P., Fauser, M., Sattlegger, D., and Steger, C. Mvtec ad—a comprehensive real-world dataset for unsupervised anomaly detection. In *Proceedings of the IEEE/CVF conference on computer vision and pattern recognition*, pp. 9592–9600, 2019.

Bergmann, P., Batzner, K., Fauser, M., Sattlegger, D., and Steger, C. The mvtec anomaly detection dataset: a comprehensive real-world dataset for unsupervised anomaly detection. *International Journal of Computer Vision*, 129(4):1038–1059, 2021a.

Bergmann, P., Jin, X., Sattlegger, D., and Steger, C. The mvtec 3d-ad dataset for unsupervised 3d anomaly detection and localization. *arXiv preprint arXiv:2112.09045*, 2021b.

Berry, E., Chen, Y.-C., Cisewski-Kehe, J., and Fasy, B. T. Functional summaries of persistence diagrams. *Journal of Applied and Computational Topology*, 4(2):211–262, 2020.

Bonneel, N. and Digne, J. A survey of optimal transport for computer graphics and computer vision. In *Computer Graphics Forum*, volume 42, pp. 439–460. Wiley Online Library, 2023.

Cao, Y., Xu, X., Zhang, J., Cheng, Y., Huang, X., Pang, G., and Shen, W. A survey on visual anomaly detection: Challenge, approach, and prospect. *arXiv preprint arXiv:2401.16402*, 2024.

Caron, M., Touvron, H., Misra, I., Jégou, H., Mairal, J., Bojanowski, P., and Joulin, A. Emerging properties in self-supervised vision transformers. In *Proceedings of the IEEE/CVF international conference on computer vision*, pp. 9650–9660, 2021.

Chen, Q., Luo, H., Lv, C., and Zhang, Z. A unified anomaly synthesis strategy with gradient ascent for industrial anomaly detection and localization. In *European Conference on Computer Vision*, pp. 37–54. Springer, 2024.

Colomer, M. B., Dovesi, P. L., Panagiotakopoulos, T., Carvalho, J. F., Härenstam-Nielsen, L., Azizpour, H., Kjellström, H., Cremers, D., and Poggi, M. To adapt or not to adapt? real-time adaptation for semantic segmentation. In *Proceedings of the IEEE/CVF International Conference on Computer Vision*, pp. 16548–16559, 2023.

Costanzino, A., Ramirez, P. Z., Del Moro, M., Aiezzo, A., Lisanti, G., Salti, S., and Di Stefano, L. Test time training for industrial anomaly segmentation. In *Proceedings of the IEEE/CVF Conference on Computer Vision and Pattern Recognition*, pp. 3910–3920, 2024a.

Costanzino, A., Ramirez, P. Z., Lisanti, G., and Di Stefano, L. Multimodal industrial anomaly detection by cross-modal feature mapping. In *Proceedings of the IEEE/CVF Conference on Computer Vision and Pattern Recognition*, pp. 17234–17243, 2024b.

Crawford, L., Monod, A., Chen, A. X., Mukherjee, S., and Rabadán, R. Predicting clinical outcomes in glioblastoma: an application of topological and functional data analysis. *Journal of the American Statistical Association*, 115(531): 1139–1150, 2020.

Cuturi, M. Sinkhorn distances: Lightspeed computation of optimal transport. *Advances in neural information processing systems*, 26, 2013.

Dan, J., Liu, W., Xie, X., Yu, H., Dong, S., and Tan, Y. Tfgda: Exploring topology and feature alignment in semi-supervised graph domain adaptation through robust clustering. *Advances in Neural Information Processing Systems*, 37:50230–50255, 2024.

Defard, T., Setkov, A., Loesch, A., and Audigier, R. Padim: a patch distribution modeling framework for anomaly detection and localization. In *International Conference on Pattern Recognition*, pp. 475–489. Springer, 2021.

Deng, H. and Li, X. Structural teacher-student normality learning for multi-class anomaly detection and localization. *arXiv preprint arXiv:2402.17091*, 2024.

Ding, C., Pang, G., and Shen, C. Catching both gray and black swans: Open-set supervised anomaly detection. In *Proceedings of the IEEE/CVF conference on computer vision and pattern recognition*, pp. 7388–7398, 2022.

Fan, Q., Shen, X., Ying, S., and Du, S. Otclda: Optimal transport and contrastive learning for domain adaptive semantic segmentation. *IEEE Transactions on Intelligent Transportation Systems*, 25(10):14685–14697, 2024.

Fang, Z., Wang, X., Li, H., Liu, J., Hu, Q., and Xiao, J. Fastrecon: Few-shot industrial anomaly detection via fast feature reconstruction. In *Proceedings of the IEEE/CVF International Conference on Computer Vision*, pp. 17481–17490, 2023.

Feydy, J., Séjourné, T., Vialard, F.-X., Amari, S.-i., Trouvé, A., and Peyré, G. Interpolating between optimal transport and mmd using sinkhorn divergences. In *The 22nd international conference on artificial intelligence and statistics*, pp. 2681–2690. PMLR, 2019.

Fučka, M., Zavrtanik, V., and Skočaj, D. Transfusion—a transparency-based diffusion model for anomaly detection. In *European conference on computer vision*, pp. 91–108. Springer, 2024.

Garside, K., Henderson, R., Makarenko, I., and Masoller, C. Topological data analysis of high resolution diabetic retinopathy images. *PloS one*, 14(5):e0217413, 2019.

Ge, Z., Liu, S., Li, Z., Yoshie, O., and Sun, J. Ota: Optimal transport assignment for object detection. In *Proceedings of the IEEE/CVF conference on computer vision and pattern recognition*, pp. 303–312, 2021.

Gu, H., Li, G., and Liu, Z. Masked feature regeneration based asymmetric student–teacher network for anomaly detection. *Multimedia Tools and Applications*, 83(42):90573–90594, 2024.

Gudovskiy, D., Ishizaka, S., and Kozuka, K. Cflow-ad: Real-time unsupervised anomaly detection with localization via conditional normalizing flows. In *Proceedings of the IEEE/CVF winter conference on applications of computer vision*, pp. 98–107, 2022.

Guo, J., Lu, S., Zhang, W., Chen, F., Li, H., and Liao, H. Dinomaly: The less is more philosophy in multi-class unsupervised anomaly detection. In *Proceedings of the Computer Vision and Pattern Recognition Conference*, pp. 20405–20415, 2025.

He, H., Bai, Y., Zhang, J., He, Q., Chen, H., Gan, Z., Wang, C., Li, X., Tian, G., and Xie, L. Mambaad: Exploring state space models for multi-class unsupervised anomaly detection. *Advances in Neural Information Processing Systems*, 37:71162–71187, 2024.

Hu, J., Huang, Y., Lu, Y., Xie, G., Jiang, G., and Zheng, Y. Anomalyxfusion: Multi-modal anomaly synthesis with diffusion. *arXiv preprint arXiv:2404.19444*, 2024a.

Hu, T., Zhang, J., Yi, R., Du, Y., Chen, X., Liu, L., Wang, Y., and Wang, C. Anomalydiffusion: Few-shot anomaly image generation with diffusion model. In *Proceedings of the AAAI Conference on Artificial Intelligence*, volume 38, pp. 8526–8534, 2024b.

Jiang, B., Xie, Y., Li, J., Li, N., Jiang, Y., and Xia, S.-T. Cagen: Controllable anomaly generator using diffusion model. In *ICASSP 2024-2024 IEEE International Conference on Acoustics, Speech and Signal Processing (ICASSP)*, pp. 3110–3114. IEEE, 2024.

Kanari, L., Dłotko, P., Scolamiero, M., Levi, R., Shillcock, J., Hess, K., and Markram, H. A topological representation of branching neuronal morphologies. *Neuroinformatics*, 16:3–13, 2018.

Khurana, A., Paul, S., Rai, P., Biswas, S., and Aggarwal, G. Sita: Single image test-time adaptation. *arXiv preprint arXiv:2112.02355*, 2021.

Kim, D., Baik, S., and Kim, T. H. Sanflow: semantic-aware normalizing flow for anomaly detection and localization. In *Proceedings of the 37th International Conference on Neural Information Processing Systems*, pp. 75434–75454, 2023.

Kim, J., Hwang, I., and Kim, Y. M. Ev-tta: Test-time adaptation for event-based object recognition. In *Proceedings of the IEEE/CVF Conference on Computer Vision and Pattern Recognition*, pp. 17745–17754, 2022.

Lei, J., Hu, X., Wang, Y., and Liu, D. Pyramidflow: High-resolution defect contrastive localization using pyramid normalizing flow. In *Proceedings of the IEEE/CVF conference on computer vision and pattern recognition*, pp. 14143–14152, 2023.

Li, W., Xu, X., Gu, Y., Zheng, B., Gao, S., and Wu, Y. Towards scalable 3d anomaly detection and localization: A benchmark via 3d anomaly synthesis and a self-supervised learning network. In *Proceedings of the IEEE/CVF conference on computer vision and pattern recognition*, pp. 22207–22216, 2024.

Li, Z., Li, N., Jiang, K., Ma, Z., Wei, X., Hong, X., and Gong, Y. Superpixel masking and inpainting for self-supervised anomaly detection. In *Bmvc*, 2020.

Liang, J., He, R., and Tan, T. A comprehensive survey on test-time adaptation under distribution shifts. *International Journal of Computer Vision*, 133(1):31–64, 2025.

Liao, J., Xu, X., Su, Y., Tu, R.-C., Liu, Y., Tao, D., and Yang, X. Robust distribution alignment for industrial anomaly detection under distribution shift. *arXiv preprint arXiv:2503.14910*, 2025.

Luo, W., Yao, H., Yu, W., and Li, Z. Ami-net: Adaptive mask inpainting network for industrial anomaly detection and localization. *IEEE Transactions on Automation Science and Engineering*, 2024.

Luo, Y.-W. and Ren, C.-X. Mot: Masked optimal transport for partial domain adaptation. In *2023 IEEE/CVF Conference on Computer Vision and Pattern Recognition (CVPR)*, pp. 3531–3540. IEEE, 2023.

Michaeli, E. and Fried, O. Advancing fine-grained classification by structure and subject preserving augmentation. *Advances in Neural Information Processing Systems*, 37: 22316–22349, 2024.

Nado, Z., Padhy, S., Sculley, D., D’Amour, A., Lakshminarayanan, B., and Snoek, J. Evaluating prediction-time batch normalization for robustness under covariate shift. *arXiv preprint arXiv:2006.10963*, 2020.

Nakanishi, H., Suzuki, M., and Matsuo, Y. Fixing the train-test objective discrepancy: Iterative image inpainting for unsupervised anomaly detection. *Journal of Information Processing*, 30:495–504, 2022.

Nguyen, A. T., Nguyen-Tang, T., Lim, S.-N., and Torr, P. H. Tipi: Test time adaptation with transformation invariance. In *Proceedings of the IEEE/CVF Conference on Computer Vision and Pattern Recognition*, pp. 24162–24171, 2023.

Oquab, M., Dariseti, T., Moutakanni, T., Vo, H., Szafraniec, M., Khalidov, V., Fernandez, P., Haziza, D., Massa, F., El-Nouby, A., et al. Dinov2: Learning robust visual features without supervision. *arXiv preprint arXiv:2304.07193*, 2023.

Park, Y., Kang, S., Kim, M. J., Jeong, H., Park, H., Kim, H. S., and Yi, J. Neural network training strategy to enhance anomaly detection performance: A perspective on reconstruction loss amplification. In *ICASSP 2024-2024 IEEE International Conference on Acoustics, Speech and Signal Processing (ICASSP)*, pp. 5165–5169. IEEE, 2024.

Peyré, G., Cuturi, M., et al. Computational optimal transport: With applications to data science. *Foundations and Trends® in Machine Learning*, 11(5-6):355–607, 2019.

Pirnay, J. and Chai, K. Inpainting transformer for anomaly detection. In *International Conference on Image Analysis and Processing*, pp. 394–406. Springer, 2022.

Qiu, L., Wu, X., and Yu, Z. A high-efficiency fully convolutional networks for pixel-wise surface defect detection. *IEEE Access*, 7:15884–15893, 2019.

Redko, I., Habrard, A., and Sebban, M. Theoretical analysis of domain adaptation with optimal transport. In *Joint European Conference on Machine Learning and Knowledge Discovery in Databases*, pp. 737–753. Springer, 2017.

Reininghaus, J., Huber, S., Bauer, U., and Kwitt, R. A stable multi-scale kernel for topological machine learning. In *Proceedings of the IEEE conference on computer vision and pattern recognition*, pp. 4741–4748, 2015.

Roth, K., Pemula, L., Zepeda, J., Schölkopf, B., Brox, T., and Gehler, P. Towards total recall in industrial anomaly detection. In *Proceedings of the IEEE/CVF conference on computer vision and pattern recognition*, pp. 14318–14328, 2022.

Rudolph, M., Wehrbein, T., Rosenhahn, B., and Wandt, B. Asymmetric student-teacher networks for industrial anomaly detection. In *Proceedings of the IEEE/CVF winter conference on applications of computer vision*, pp. 2592–2602, 2023.

Sun, Y., Wang, X., Liu, Z., Miller, J., Efros, A., and Hardt, M. Test-time training with self-supervision for generalization under distribution shifts. In *International conference on machine learning*, pp. 9229–9248. PMLR, 2020.

Tao, X., Gong, X., Zhang, X., Yan, S., and Adak, C. Deep learning for unsupervised anomaly localization in industrial images: A survey. *IEEE Transactions on Instrumentation and Measurement*, 71:1–21, 2022.

Tong, G., Li, Q., and Song, Y. Enhanced multi-scale features mutual mapping fusion based on reverse knowledge distillation for industrial anomaly detection and localization. *IEEE Transactions on Big Data*, 10(4):498–513, 2024.

Turner, K., Mileyko, Y., Mukherjee, S., and Harer, J. Fréchet means for distributions of persistence diagrams. *Discrete & Computational Geometry*, 52(1):44–70, 2014.

Volpi, R., De Jorge, P., Larlus, D., and Csurka, G. On the road to online adaptation for semantic image segmentation. In *Proceedings of the IEEE/CVF conference on computer vision and pattern recognition*, pp. 19184–19195, 2022.

Wang, C., Zhu, W., Gao, B.-B., Gan, Z., Zhang, J., Gu, Z., Qian, S., Chen, M., and Ma, L. Real-iad: A real-world

multi-view dataset for benchmarking versatile industrial anomaly detection. In *Proceedings of the IEEE/CVF Conference on Computer Vision and Pattern Recognition*, pp. 22883–22892, 2024a.

Wang, J., Xu, G., Li, C., Gao, G., and Cheng, Y. Multi-feature reconstruction network using crossed-mask restoration for unsupervised anomaly detection. *arXiv preprint arXiv:2404.13273*, 2024b.

Wang, Y., Peng, J., Zhang, J., Yi, R., Wang, Y., and Wang, C. Multimodal industrial anomaly detection via hybrid fusion. In *Proceedings of the IEEE/CVF Conference on Computer Vision and Pattern Recognition*, pp. 8032–8041, 2023.

Wu, Q., Li, H., Tian, C., Wen, L., and Li, X. Aekd: Unsupervised auto-encoder knowledge distillation for industrial anomaly detection. *Journal of Manufacturing Systems*, 73:159–169, 2024.

Xie, X. and Mirmehdi, M. Texems: Texture exemplars for defect detection on random textured surfaces. *IEEE transactions on pattern analysis and machine intelligence*, 29(8):1454–1464, 2007.

Yao, H., Liu, M., Yin, Z., Yan, Z., Hong, X., and Zuo, W. Glad: Towards better reconstruction with global and local adaptive diffusion models for unsupervised anomaly detection. In *European Conference on Computer Vision*, pp. 1–17. Springer, 2024a.

Yao, X., Li, R., Qian, Z., Wang, L., and Zhang, C. Hierarchical gaussian mixture normalizing flow modeling for unified anomaly detection. In *European Conference on Computer Vision*, pp. 92–108. Springer, 2024b.

Ye, J., Zhao, W., Yang, X., Cheng, G., and Huang, K. Po3ad: Predicting point offsets toward better 3d point cloud anomaly detection. In *Proceedings of the Computer Vision and Pattern Recognition Conference*, pp. 1353–1362, 2025.

Zavrtanik, V., Kristan, M., and Skočaj, D. Reconstruction by inpainting for visual anomaly detection. *Pattern Recognition*, 112:107706, 2021a.

Zavrtanik, V., Kristan, M., and Skočaj, D. Draem – a discriminatively trained reconstruction embedding for surface anomaly detection. In *IEEE/CVF International Conference on Computer Vision (ICCV)*, pp. 8330–8339, 2021b.

Zhang, X., Li, S., Li, X., Huang, P., Shan, J., and Chen, T. Destseg: Segmentation guided denoising student-teacher for anomaly detection. In *Proceedings of the IEEE/CVF Conference on Computer Vision and Pattern Recognition*, pp. 3914–3923, 2023.

Zhang, X., Hong, B.-W., Park, H., Pak, D. H., Rickmann, A.-M., Staib, L. H., Duncan, J. S., and Wong, A. Progressive test time energy adaptation for medical image segmentation. *arXiv preprint arXiv:2503.16616*, 2025.

Zhang, Y., Hooi, B., Hong, L., and Feng, J. Self-supervised aggregation of diverse experts for test-agnostic long-tailed recognition. *Advances in Neural Information Processing Systems*, 35:34077–34090, 2022.

Zhao, C., Zio, E., and Shen, W. Domain generalization for cross-domain fault diagnosis: An application-oriented perspective and a benchmark study. *Reliability Engineering & System Safety*, pp. 109964, 2024.

Zhao, H., Jiang, L., Jia, J., Torr, P. H., and Koltun, V. Point transformer. In *Proceedings of the IEEE/CVF international conference on computer vision*, pp. 16259–16268, 2021.

Zhou, Y., Xu, X., Song, J., Shen, F., and Shen, H. T. Msflow: Multiscale flow-based framework for unsupervised anomaly detection. *IEEE Transactions on Neural Networks and Learning Systems*, 2024a.

Zhou, Z., Wang, L., Fang, N., Wang, Z., Qiu, L., and Zhang, S. R3d-ad: Reconstruction via diffusion for 3d anomaly detection. In *European conference on computer vision*, pp. 91–107. Springer, 2024b.

Zhu, J., Ding, C., Tian, Y., and Pang, G. Anomaly heterogeneity learning for open-set supervised anomaly detection. In *Proceedings of the IEEE/CVF Conference on Computer Vision and Pattern Recognition*, pp. 17616–17626, 2024.

Zia, A., Khamis, A., Nichols, J., Tayab, U. B., Hayder, Z., Rolland, V., Stone, E., and Petersson, L. Topological deep learning: a review of an emerging paradigm. *Artificial Intelligence Review*, 57(4):77, 2024.

Zou, Y., Jeong, J., Pemula, L., Zhang, D., and Dabeer, O. Spot-the-difference self-supervised pre-training for anomaly detection and segmentation. In *European conference on computer vision*, pp. 392–408. Springer, 2022.

Zuo, Z., Wu, Z., Chen, B., and Zhong, X. A reconstruction-based feature adaptation for anomaly detection with self-supervised multi-scale aggregation. In *ICASSP 2024-2024 IEEE International Conference on Acoustics, Speech and Signal Processing (ICASSP)*, pp. 5840–5844. IEEE, 2024.

A. Supplementary Material

- A.1 outlines the *experimental setup* for 2D and 3D anomaly detection with test-time adaptation and hyperparameter configuration.
- A.2 evaluate the *computational efficiency* of TopoOT by benchmarking its inference time and GPU memory usage in 2D and 3D AS scenarios.
- A.3 discuss *fundamental insights, limitations, and possible extensions* within the context of topological anomaly segmentation.
- A.4 presents *quantitative and qualitative results* on 2D AD&S datasets, including class-wise performance across benchmarks and visual examples that illustrate the effectiveness of OT-guided pseudo-labels.
- A.5 reports *quantitative and qualitative results* on 3D AD&S datasets, covering point-cloud modalities, with class-level analysis and qualitative comparisons to baseline methods.
- A.6 recalls *optimal transport preliminaries*, including the 2-Wasserstein distance and its entropy-regularised Sinkhorn variant, and clarifies their role in computing the OT couplings used in our framework.
- A.7 provides a conceptual motivation into optimal transport stability and behaviour.
- A.8 presents the *mathematical formulation* of cubical complex persistence, detailing how primitive cells are hierarchically aggregated to construct filtration levels and ultimately generate persistence vectors that encode topological features.
- A.9 shows the *ablation study* on the Top- K persistence components, highlighting how varying K impacts the evaluation metrics and that adding lower-ranked components tends to introduce noise and degrade performance.
- A.10 provides a *qualitative analysis* of challenging textural anomaly cases, illustrating how the proposed topology-guided pseudo-labels behave when the backbone anomaly maps exhibit weak topological structure.
- A.11 provides the *complete algorithmic pseudocode* for TopoOT, formally defining the multi-scale filtration steps, stability-aware OT chaining, and the spatial backtracking mechanism that drives the test-time adaptation loop.

A.1. Architectural Settings & Hyperparameters

2D Setup. For all RGB-based AD&S experiments, we employ **DINO** (Caron et al., 2021) as the feature extractor (F). Our approach is benchmarked against leading state-of-the-art methods, including the memory-bank based **PatchCore** (Roth et al., 2022), **PaDiM** (Defard et al., 2021), the reconstruction-driven **Dinomaly** (Guo et al., 2025), and **MambaAD** (He et al., 2024). Evaluation is conducted on three widely adopted 2D benchmarks: **MVTec AD** (Bergmann et al., 2019) (15 categories; 3,629 training and 1,725 test images), **VisA** (Zou et al., 2022) (12 objects; 9,621 normal and 1,200 anomalous samples), and **Real-IAD** (Wang et al., 2024a) (30 objects; \sim 150,000 images in total, comprising 36,465 normal training samples and 114,585 test images with 63,256 normal and 51,329 anomalous). To ensure comparability, all 2D inputs are standardised to a resolution of 224×224 .

3D Setup. For multimodal experiments involving RGB and point-cloud modalities, we adopt **DINO-v2** (Oquab et al., 2023) for image features and **Point-MAE** (Zhao et al., 2021) for geometric representations. We benchmark against multimodal memory-bank methods such as **M3DM** (Wang et al., 2023), as well as reconstruction-oriented baselines including **CMM** (Costanzino et al., 2024b) and **PO3AD** (Ye et al., 2025). The evaluation is performed on two representative 3D benchmarks: **MVTec 3D-AD** (Bergmann et al., 2021b) (10 categories; 2,656 nominal training images and 1,197 test samples) and **Anomaly-ShapeNet** (Li et al., 2024) (40 synthetic classes; 1,600 samples spanning six anomaly types).

Test-Time Training. For adaptation, the pretrained backbones are kept frozen while a lightweight MLP head h_ψ , consisting of three linear layers with GELU activations, is fine-tuned. The optimisation objective combines an OT-consistency loss ($\epsilon = 0.05$, up to 200 iterations) with a contrastive loss (margin = 0.4), balanced equally with weights $\alpha = \lambda = 0.5$. Adaptation proceeds for 5 epochs using the Adam optimiser with a learning rate of 10^{-3} . Each test sample is processed independently with an effective batch size of one.

A.2. Computational Complexity and Efficiency

A central strength of the proposed **TopoOT** framework lies in its ability to balance computational complexity with practical efficiency. When evaluated on a single modern GPU, the *complete end-to-end* TopoOT pipeline operates at approximately **2.90 FPS**, while the lightweight **TTT** module alone achieves **121 FPS**. Notably, the **OT** and **TDA** components currently run exclusively on the **CPU**, which constrains the overall end-to-end throughput, while requiring only **349 MB** of GPU memory. This lightweight profile is markedly lower than that of many SOTA anomaly detection baselines. For context, a standard 2D baseline model (Roth et al., 2022) reports an inference time of 0.22 seconds per image, while in the 3D domain, the M3DM (Wang et al., 2023) model requires 2.86 seconds per image and consumes 6.52 GB of GPU memory. The CMM (Costanzino et al., 2024b) model, though faster at 0.12 seconds per image, still uses 427 MB of memory. **TopoOT** delivers a $14.5 \times$ speedup over CMM. In contrast, **TopoOT** not only achieves a significantly higher frame rate but also maintains a highly competitive memory footprint, underscoring its deployability in scenarios where throughput and hardware constraints are decisive.

The breakdown of computational cost, analysed per module, indicates that the construction of cubical complexes and persistence diagrams constitutes the most demanding stage, requiring approximately **0.33 seconds** per sample when aggregated across all complexes. Despite this initial overhead, the subsequent topological alignment stages remain highly efficient: the *intra-level OT* block requires only **5.5 ms** in aggregate, while the *inter-level OT* block converges nearly instantaneously, below **0.05 ms** per alignment. These operations stabilise and align persistence features without imposing a significant runtime burden. Finally, the downstream multilayer perceptron (MLP) classifier adds only **8.3 ms** per evaluation, rendering its contribution negligible.

Table 4 summarises the per-sample runtime for each backbone, split into backbone inference, persistence diagram (PD) computation, OT alignment and the TopoOT TTT head. The PD stage is the main overhead, while OT and TTT are negligible (the TTT head adds only 0.008 s), so the overall end-to-end latency remains comparable to or better than existing 2D/3D anomaly detection baselines.

Table 4. Backbone processing time, TTT method time per sample, and total time (all in seconds).

| Method | Backbone | | TopoOT | | | | Total | |
|---------------------------------------|--------------------|-------------|--------|--------|---------|-------------|----------|-------------|
| | Inference Time (s) | Memory (GB) | PD (s) | OT (s) | TTT (s) | Memory (GB) | Time (s) | Memory (GB) |
| PaDiM (Defard et al., 2021) | 0.950 | 2.100 | 0.325 | 0.005 | 0.008 | 0.349 | 1.288 | 2.449 |
| Patchcore (Roth et al., 2022) | 0.223 | 3.450 | 0.331 | 0.006 | 0.008 | 0.349 | 0.568 | 3.799 |
| M3DM (Wang et al., 2023) | 2.862 | 6.520 | 0.349 | 0.006 | 0.008 | 0.417 | 3.225 | 6.937 |
| CMM (Costanzino et al., 2024b) | 0.124 | 0.427 | 0.352 | 0.006 | 0.008 | 0.417 | 0.490 | 0.844 |
| MambaAD (He et al., 2024) | 0.027 | 1.480 | 0.374 | 0.006 | 0.008 | 0.370 | 0.415 | 1.850 |
| Dinomaly (Guo et al., 2025) | 0.041 | 4.320 | 0.392 | 0.006 | 0.008 | 0.370 | 0.447 | 4.690 |
| PO3AD (Ye et al., 2025) | 0.294 | 1.950 | 0.397 | 0.006 | 0.008 | 0.495 | 0.705 | 2.446 |

Taken together, the end-to-end evaluation time per sample remains well within practical limits, supporting real-time operation. The combination of **high FPS**, **minimal GPU consumption**, and the bounded cost of topological computations makes **TopoOT** exceptionally well-suited for industrial adoption. Unlike competing methods that often trade accuracy for efficiency, **TopoOT** achieves both, offering a robust and scalable solution for anomaly detection under stringent practical constraints.

A.3. Discussion, Limitations, and Future Directions

The results in the main paper and Appendices A.4 A.5 demonstrate that TopoOT provides a principled strategy for replacing non-robust and heuristic thresholding with stability-aware, OT-guided pseudo-labels. By chaining persistence diagrams across filtrations and integrating sub- and super-level information, the framework yields segmentation masks that are both structurally coherent and robust under distribution shift. Consistent gains across 2D and 3D benchmarks confirm that structural alignment is an effective prior for test-time adaptation.

Despite these advances, several limitations remain. First, the approach still depends on the quality of the anomaly score maps produced by frozen backbones. When upstream representations are noisy or poorly transferable, the extracted persistent features may not provide sufficient structural guidance. Second, while the current formulation generalises naturally to both 2D images and 3D point clouds, it does not yet address spatiotemporal settings such as video or dynamic medical imaging,

where temporal coherence and evolving anomaly structure are critical. Third, efficiency trade-offs deserve further study, although TopoOT is lightweight relative to baselines, scaling to real-time, high-resolution deployments in safety-critical domains may require additional optimisations.

Future work can address these challenges along several directions. Differentiable approximations of persistent homology offer a path to end-to-end training with topological losses, enabling tighter integration between backbone features and topological stability. Jointly optimising anomaly map generation and topological filtering through self-supervised objectives could mitigate the reliance on noisy upstream scores. Extending the framework to spatiotemporal domains will require evolving persistence diagrams across frames to capture anomaly lifespans and enforce temporal consistency. Finally, incorporating uncertainty-aware filtration strategies, quantifying stability not only by persistence but also by variability across augmentations or agreement with model uncertainty, could provide more reliable predictions in high-stakes applications such as robotics, autonomous driving, and medical diagnostics.

TopoOT establishes a solid foundation for topology-aware adaptation in anomaly segmentation, highlighting how persistent homology and optimal transport can jointly serve as structural alignment mechanisms for adaptive learning. Its current form addresses critical limitations of threshold-based methods, while future developments promise broader applicability and deeper integration with modern representation learning.

A.4. Additional Experiments and Results on 2D AD&S Datasets

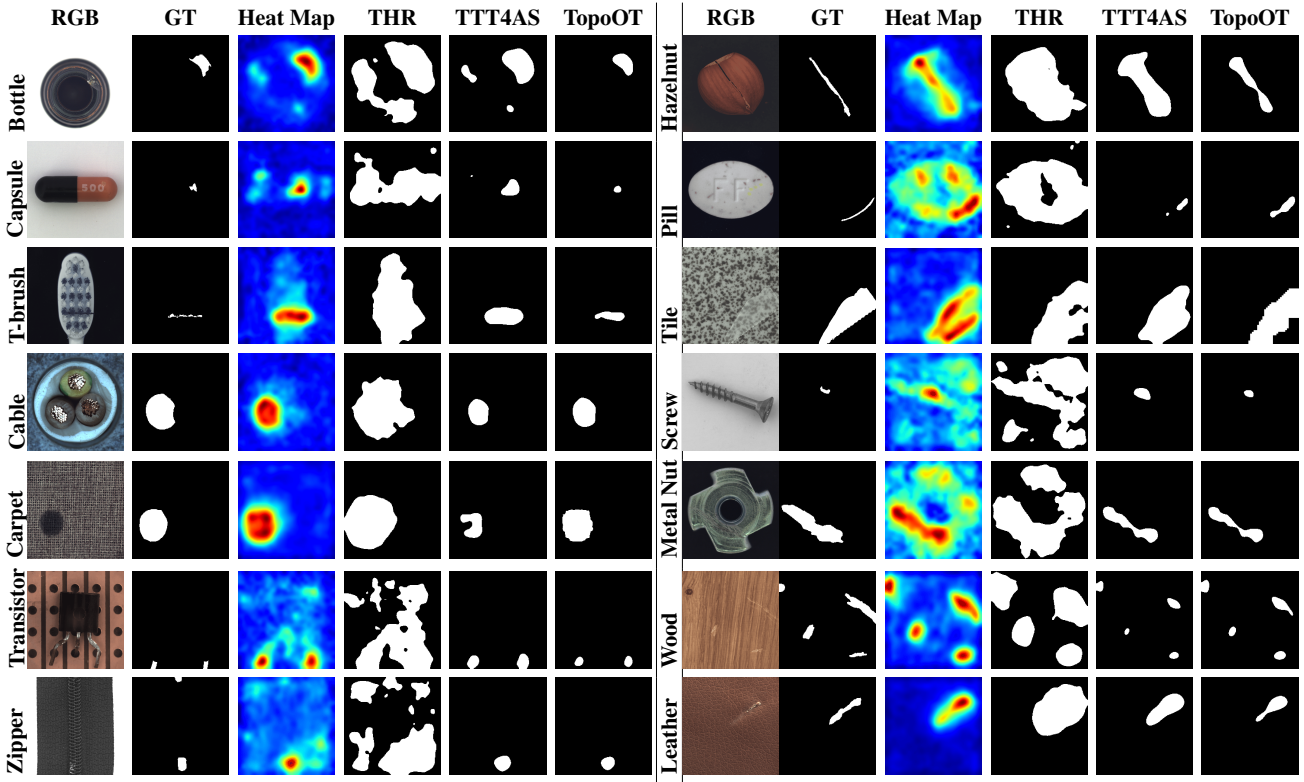


Figure 3. Qualitative comparison of various anomaly detection methods for different objects using backbone PatchCore on 2D MvTec AD dataset.

Qualitative results in PatchCore backbone using the 2D MvTec AD dataset are shown in Figure 3. Table 5 reports the results of PatchCore on the MvTec AD dataset, evaluated using I-AUROC, P-AUROC, and P-AUPRO. These results are reproduced directly using the official implementation provided by the authors.

The comparative analysis in Table 6 details the effectiveness of various binary segmentation approaches on MvTec AD. By leveraging topological priors, TopoOT yields substantial performance gains over the THR and TTT4AS baselines, maintaining a superior margin across all 15 categories and all reported metrics.

Table 5. PatchCore (Roth et al., 2022) on MVTec AD: anomaly scores are I-AUROC, P-AUROC, and P-AUPRO.

| Metric | Bottle | Cable | Capsule | Carpet | Grid | Hazelnut | Leather | MetalNut | Pill | Screw | Tile | T-brush | Transistor | Wood | Zipper | Mean |
|--|--------|-------|---------|--------|-------|----------|---------|----------|-------|-------|-------|---------|------------|-------|--------|-------|
| PatchCore — Anomaly Scores (Roth et al., 2022) | | | | | | | | | | | | | | | | |
| | | | | | | | | | | | | | | | | |
| I-AUROC | 1.000 | 0.995 | 0.981 | 0.987 | 0.982 | 1.000 | 1.000 | 0.966 | 0.981 | 0.987 | 1.000 | 1.000 | 0.992 | 0.994 | 0.991 | |
| P-AUROC | 0.986 | 0.984 | 0.988 | 0.990 | 0.987 | 0.987 | 0.993 | 0.984 | 0.974 | 0.994 | 0.956 | 0.987 | 0.963 | 0.950 | 0.988 | 0.981 |
| P-AUPRO | 0.961 | 0.926 | 0.955 | 0.966 | 0.959 | 0.939 | 0.989 | 0.913 | 0.941 | 0.979 | 0.874 | 0.914 | 0.835 | 0.896 | 0.971 | 0.935 |

 Table 6. Performance of PatchCore (Roth et al., 2022) on MVTec AD’s 15 categories, comparing binary map strategies: THR ($\mu + 3\sigma$), TTT4AS, and TopoOT. Top results per metric are in **bold** (best) and **blue** (second-best).

| Metric | Bottle | Cable | Capsule | Carpet | Grid | Hazelnut | Leather | MetalNut | Pill | Screw | Tile | T-brush | Transistor | Wood | Zipper | Mean |
|--|--------------|--------------|--------------|--------------|--------------|--------------|--------------|--------------|--------------|--------------|--------------|--------------|--------------|--------------|--------------|--------------|
| (a) PatchCore - Binary Map - THR ($\mu + 3\sigma$) (Roth et al., 2022) | | | | | | | | | | | | | | | | |
| | | | | | | | | | | | | | | | | |
| Precision | 0.397 | 0.344 | 0.278 | 0.362 | 0.432 | 0.405 | 0.297 | 0.435 | 0.347 | 0.298 | 0.403 | 0.286 | 0.334 | 0.384 | 0.268 | 0.351 |
| Recall | 0.510 | 0.465 | 0.626 | 0.522 | 0.428 | 0.380 | 0.542 | 0.566 | 0.618 | 0.522 | 0.517 | 0.542 | 0.287 | 0.469 | 0.605 | 0.507 |
| F1 Score | 0.175 | 0.194 | 0.085 | 0.092 | 0.078 | 0.120 | 0.045 | 0.311 | 0.188 | 0.066 | 0.209 | 0.123 | 0.114 | 0.121 | 0.119 | 0.136 |
| IoU | 0.310 | 0.334 | 0.222 | 0.407 | 0.283 | 0.367 | 0.262 | 0.316 | 0.287 | 0.202 | 0.179 | 0.262 | 0.238 | 0.297 | 0.513 | 0.299 |
| (b) PatchCore - Binary Map - TTT4AS (Costanzino et al., 2024a) | | | | | | | | | | | | | | | | |
| | | | | | | | | | | | | | | | | |
| Precision | 0.662 | 0.502 | 0.163 | 0.413 | 0.185 | 0.425 | 0.212 | 0.644 | 0.337 | 0.046 | 0.644 | 0.272 | 0.391 | 0.470 | 0.449 | 0.388 |
| Recall | 0.664 | 0.565 | 0.632 | 0.824 | 0.787 | 0.861 | 0.893 | 0.528 | 0.740 | 0.361 | 0.495 | 0.594 | 0.462 | 0.664 | 0.644 | 0.648 |
| F1 Score | 0.593 | 0.480 | 0.197 | 0.457 | 0.272 | 0.499 | 0.286 | 0.482 | 0.358 | 0.078 | 0.474 | 0.301 | 0.318 | 0.464 | 0.469 | 0.382 |
| IoU | 0.358 | 0.393 | 0.166 | 0.379 | 0.243 | 0.418 | 0.208 | 0.276 | 0.264 | 0.124 | 0.404 | 0.234 | 0.192 | 0.360 | 0.370 | 0.293 |
| (c) PatchCore - Binary Map - TopoOT | | | | | | | | | | | | | | | | |
| | | | | | | | | | | | | | | | | |
| Precision | 0.850 | 0.673 | 0.399 | 0.625 | 0.370 | 0.487 | 0.392 | 0.717 | 0.416 | 0.282 | 0.713 | 0.390 | 0.581 | 0.595 | 0.765 | 0.550 |
| Recall | 0.555 | 0.672 | 0.772 | 0.685 | 0.741 | 0.869 | 0.909 | 0.709 | 0.787 | 0.890 | 0.643 | 0.647 | 0.496 | 0.579 | 0.640 | 0.720 |
| F1 Score | 0.623 | 0.627 | 0.445 | 0.545 | 0.458 | 0.579 | 0.493 | 0.654 | 0.465 | 0.396 | 0.627 | 0.412 | 0.440 | 0.527 | 0.646 | 0.522 |
| IoU | 0.474 | 0.476 | 0.307 | 0.400 | 0.314 | 0.429 | 0.356 | 0.507 | 0.333 | 0.269 | 0.493 | 0.271 | 0.301 | 0.381 | 0.495 | 0.387 |

Specifically, in terms of mean performance, **TopoOT** achieves an F1 Score of 0.522, significantly higher than THR (0.136) and TTT4AS (0.382). This corresponds to a relative improvement of **+0.386** over THR and **+0.140** over TTT4AS. Similarly, in terms of Precision, TopoOT improves over THR and TTT4AS by **+0.199** and **+0.162**, respectively. A comparable trend is observed for Recall, where TopoOT provides a gain of **+0.213** over THR and **+0.072** over TTT4AS. Beyond overall averages, significant category-level improvements can also be observed in Table 6.

Table 7 presents the performance of PaDiM on the MVTec AD dataset, evaluated using I-AUROC, P-AUROC, and P-AUPRO. The reported results are reproduced directly from the official implementation released by the authors.

Table 7. PaDiM (Defard et al., 2021) on MVTec AD: anomaly scores are I-AUROC, P-AUROC and P-AUPRO.

| Metric | Bottle | Cable | Capsule | Carpet | Grid | Hazelnut | Leather | MetalNut | Pill | Screw | Tile | T-brush | Transistor | Wood | Zipper | Mean |
|---------|--------|-------|---------|--------|-------|----------|---------|----------|-------|-------|-------|---------|------------|-------|--------|-------|
| I-AUROC | 0.971 | 0.982 | 0.974 | 0.979 | 0.995 | 0.991 | 0.965 | 0.942 | 0.995 | 0.972 | 0.961 | 0.929 | 0.973 | 0.984 | 0.957 | 0.979 |
| P-AUROC | 0.983 | 0.967 | 0.985 | 0.991 | 0.973 | 0.982 | 0.992 | 0.972 | 0.957 | 0.985 | 0.941 | 0.988 | 0.975 | 0.949 | 0.985 | 0.975 |
| P-AUPRO | 0.948 | 0.888 | 0.935 | 0.962 | 0.946 | 0.926 | 0.978 | 0.856 | 0.927 | 0.944 | 0.860 | 0.931 | 0.845 | 0.911 | 0.959 | 0.921 |

Table 8 details a comparative analysis of the PaDiM architecture on the MVTec AD benchmark across diverse binarization paradigms. Our proposed method, **TopoOT**, yields consistent performance gains over both the baseline thresholding (THR) and the state-of-the-art TTT4AS. Specifically, TopoOT achieves a significant average increase in F1 Score of **+0.205** and **+0.241** compared to THR and TTT4AS, respectively. This trend extends to Precision, with improvements of **+0.018** (vs. THR) and **+0.14** (vs. TTT4AS). The most substantial gains are observed in Recall, where TopoOT surpasses THR by **+0.281** and TTT4AS by **+0.209**, demonstrating its superior capability in capturing complex anomaly geometries.

Table 9 presents the results of MambaAD on VisA (12 classes), where I-AUROC, P-AUROC, and P-AUPRO are reported as **mean per class**. The results are reproduced directly using the official implementation provided by the authors.

Table 10 illustrates the comparative performance of MambaAD on the VisA dataset across 12 distinct categories under various binary segmentation frameworks. Our proposed method, **TopoOT**, yields consistent advancements in both Precision and F1 Score relative to the THR and TTT4AS baselines. Specifically, TopoOT enhances the average F1 Score by **+0.111** and **+0.085** over THR and TTT4AS, respectively, while Precision exhibits substantial growth of **+0.216** (vs. THR) and **+0.193** (vs. TTT4AS). While TopoOT shows a marginal reduction in Recall, this is a direct result of the method’s ability to

Table 8. Performance evaluation of PaDiM (Defard et al., 2021) across 15 categories of the MVTec AD dataset and their mean, comparing three binary map strategies: (a) THR ($\mu + 3\sigma$), (b) TTT4AS, and (c) TopoOT. The table highlights the best result for each Precision, Recall, F1 Score, and IoU in **bold** (best) and **blue** (second-best).

| Metric | Bottle | Cable | Capsule | Carpet | Grid | Hazelnut | Leather | MetalNut | Pill | Screw | Tile | T-brush | Transistor | Wood | Zipper | Mean |
|--|--------------|--------------|--------------|--------------|--------------|--------------|--------------|--------------|--------------|--------------|--------------|--------------|--------------|--------------|--------------|--------------|
| (a) PaDiM - Binary Map - THR ($\mu + 3\sigma$) (Defard et al., 2021) | | | | | | | | | | | | | | | | |
| | | | | | | | | | | | | | | | | |
| Precision | 0.729 | 0.580 | 0.287 | 0.561 | 0.327 | 0.586 | 0.306 | 0.540 | 0.410 | 0.196 | 0.131 | 0.416 | 0.462 | 0.576 | 0.676 | 0.452 |
| Recall | 0.321 | 0.249 | 0.813 | 0.736 | 0.708 | 0.477 | 0.927 | 0.281 | 0.493 | 0.712 | 0.005 | 0.514 | 0.349 | 0.399 | 0.615 | 0.507 |
| F1 Score | 0.343 | 0.280 | 0.325 | 0.523 | 0.407 | 0.433 | 0.396 | 0.292 | 0.337 | 0.295 | 0.009 | 0.391 | 0.307 | 0.375 | 0.596 | 0.354 |
| IoU | 0.310 | 0.290 | 0.330 | 0.340 | 0.320 | 0.300 | 0.310 | 0.330 | 0.320 | 0.300 | 0.280 | 0.350 | 0.330 | 0.310 | 0.335 | 0.317 |
| (b) PaDiM - Binary Map - TTT4AS (Costanzino et al., 2024a) | | | | | | | | | | | | | | | | |
| | | | | | | | | | | | | | | | | |
| Precision | 0.585 | 0.412 | 0.176 | 0.429 | 0.199 | 0.349 | 0.208 | 0.519 | 0.269 | 0.088 | 0.137 | 0.258 | 0.472 | 0.355 | 0.499 | 0.330 |
| Recall | 0.438 | 0.500 | 0.707 | 0.769 | 0.726 | 0.637 | 0.916 | 0.491 | 0.568 | 0.735 | 0.123 | 0.595 | 0.425 | 0.416 | 0.648 | 0.579 |
| F1 Score | 0.429 | 0.395 | 0.214 | 0.459 | 0.290 | 0.376 | 0.293 | 0.386 | 0.262 | 0.153 | 0.103 | 0.283 | 0.291 | 0.319 | 0.512 | 0.318 |
| IoU | 0.280 | 0.270 | 0.280 | 0.270 | 0.260 | 0.310 | 0.270 | 0.280 | 0.270 | 0.270 | 0.260 | 0.280 | 0.270 | 0.270 | 0.270 | 0.274 |
| (c) PaDiM - Binary Map - TopoOT | | | | | | | | | | | | | | | | |
| | | | | | | | | | | | | | | | | |
| Precision | 0.750 | 0.648 | 0.355 | 0.523 | 0.463 | 0.358 | 0.246 | 0.574 | 0.307 | 0.266 | 0.685 | 0.268 | 0.492 | 0.439 | 0.678 | 0.470 |
| Recall | 0.689 | 0.670 | 0.828 | 0.942 | 0.805 | 0.885 | 0.987 | 0.636 | 0.783 | 0.905 | 0.742 | 0.920 | 0.547 | 0.756 | 0.724 | 0.788 |
| F1 Score | 0.718 | 0.658 | 0.496 | 0.672 | 0.587 | 0.509 | 0.393 | 0.603 | 0.441 | 0.411 | 0.712 | 0.415 | 0.518 | 0.555 | 0.700 | 0.559 |
| IoU | 0.390 | 0.410 | 0.400 | 0.420 | 0.380 | 0.400 | 0.410 | 0.390 | 0.400 | 0.410 | 0.420 | 0.390 | 0.410 | 0.400 | 0.400 | 0.402 |

Table 9. MambaAD (He et al., 2024) on VisA (12 classes), I-AUROC, P-AUROC, P-AUPRO, metrics are **mean per class**.

| Metric | candle | capsules | cashew | chewinggum | fryum | macaroni1 | macaroni2 | pcb1 | pcb2 | pcb3 | pcb4 | pipe_fryum | Mean |
|---------|--------|----------|--------|------------|-------|-----------|-----------|-------|-------|-------|-------|------------|-------|
| I-AUROC | 0.968 | 0.918 | 0.945 | 0.977 | 0.952 | 0.916 | 0.816 | 0.954 | 0.942 | 0.937 | 0.999 | 0.987 | 0.943 |
| P-AUROC | 0.990 | 0.991 | 0.943 | 0.981 | 0.969 | 0.995 | 0.995 | 0.998 | 0.989 | 0.991 | 0.986 | 0.991 | 0.985 |
| P-AUPRO | 0.955 | 0.918 | 0.878 | 0.797 | 0.916 | 0.952 | 0.962 | 0.928 | 0.896 | 0.891 | 0.876 | 0.951 | 0.910 |

Table 10. Performance evaluation of MambaAD (He et al., 2024) 12 categories (VisA classes) and their mean, comparing three binary map strategies: (a) THR ($\mu + 3\sigma$), (b) TTT4AS, and (c) TopoOT. The table highlights the best result for each Precision, Recall, and F1 Score metric in **bold black** and the second-best in **blue**.

| Metric | candle | capsules | cashew | chewinggum | fryum | macaroni1 | macaroni2 | pcb1 | pcb2 | pcb3 | pcb4 | pipe_fryum | Mean |
|--|--------------|--------------|--------------|--------------|--------------|--------------|--------------|--------------|--------------|--------------|--------------|--------------|--------------|
| (a) MambaAD - Binary Map - THR ($\mu + 3\sigma$) (He et al., 2024) | | | | | | | | | | | | | |
| | | | | | | | | | | | | | |
| Precision | 0.111 | 0.291 | 0.163 | 0.368 | 0.265 | 0.049 | 0.060 | 0.224 | 0.166 | 0.209 | 0.333 | 0.166 | 0.200 |
| Recall | 0.874 | 0.741 | 0.699 | 0.796 | 0.659 | 0.775 | 0.804 | 0.954 | 0.816 | 0.779 | 0.648 | 0.877 | 0.785 |
| F1 Score | 0.172 | 0.357 | 0.174 | 0.468 | 0.207 | 0.088 | 0.104 | 0.278 | 0.255 | 0.299 | 0.396 | 0.092 | 0.241 |
| IoU | 0.105 | 0.259 | 0.105 | 0.334 | 0.127 | 0.048 | 0.058 | 0.278 | 0.255 | 0.299 | 0.396 | 0.092 | 0.196 |
| (b) MambaAD - Binary Map - TTT4AS (Guo et al., 2025) | | | | | | | | | | | | | |
| | | | | | | | | | | | | | |
| Precision | 0.185 | 0.389 | 0.229 | 0.335 | 0.263 | 0.079 | 0.052 | 0.239 | 0.235 | 0.243 | 0.398 | 0.178 | 0.235 |
| Recall | 0.807 | 0.879 | 0.857 | 0.867 | 0.716 | 0.807 | 0.858 | 0.889 | 0.824 | 0.822 | 0.601 | 0.918 | 0.820 |
| F1 Score | 0.264 | 0.440 | 0.275 | 0.484 | 0.190 | 0.137 | 0.097 | 0.307 | 0.339 | 0.331 | 0.419 | 0.186 | 0.289 |
| IoU | 0.104 | 0.258 | 0.114 | 0.331 | 0.113 | 0.032 | 0.025 | 0.163 | 0.122 | 0.167 | 0.217 | 0.095 | 0.145 |
| (c) MambaAD - Binary Map - TopoOT | | | | | | | | | | | | | |
| | | | | | | | | | | | | | |
| Precision | 0.311 | 0.483 | 0.336 | 0.577 | 0.444 | 0.198 | 0.184 | 0.507 | 0.431 | 0.480 | 0.702 | 0.341 | 0.416 |
| Recall | 0.542 | 0.460 | 0.563 | 0.573 | 0.290 | 0.565 | 0.664 | 0.529 | 0.410 | 0.469 | 0.317 | 0.696 | 0.507 |
| F1 Score | 0.295 | 0.357 | 0.314 | 0.528 | 0.199 | 0.247 | 0.258 | 0.462 | 0.388 | 0.433 | 0.392 | 0.346 | 0.352 |
| IoU | 0.196 | 0.246 | 0.217 | 0.394 | 0.200 | 0.157 | 0.163 | 0.328 | 0.267 | 0.298 | 0.267 | 0.226 | 0.247 |

Table 11. Dinomaly (Guo et al., 2025) on VisA (12 classes). Anomaly scores I-AUROC, P-AUROC and P-AUPRO.

| Metric | candle | capsules | cashew | chewinggum | fryum | macaroni1 | macaroni2 | pcb1 | pcb2 | pcb3 | pcb4 | pipe_fryum | Mean |
|---|--------|----------|--------|------------|-------|-----------|-----------|-------|-------|-------|-------|------------|-------|
| (a) Dinomaly (Guo et al., 2025) - Anomaly Score | | | | | | | | | | | | | |
| | | | | | | | | | | | | | |
| I-AUROC | 0.987 | 0.986 | 0.987 | 0.998 | 0.988 | 0.980 | 0.959 | 0.991 | 0.993 | 0.989 | 0.998 | 0.992 | 0.987 |
| P-AUROC | 0.994 | 0.996 | 0.971 | 0.991 | 0.966 | 0.996 | 0.997 | 0.995 | 0.980 | 0.984 | 0.987 | 0.992 | 0.987 |
| P-AUPRO | 0.954 | 0.974 | 0.940 | 0.881 | 0.935 | 0.964 | 0.987 | 0.951 | 0.913 | 0.946 | 0.944 | 0.952 | 0.945 |

Table 12. MambaAD (He et al., 2024) on Real-IAD (30 classes). Anomaly scores I-AUROC, P-AUROC and P-AUPRO.

| Metric | audiojack | b-cap | b-battery | e-cap | eraser | f-hood | mint | mounts | pcb | p-battery | p-nut | p-plug | p-doll | regulator | r-base | s-set | | |
|--|-----------|-------|-----------|---------|--------|---------|-------------|---------|-------|-----------|--------|---------|-----------|-----------|--------|-------|--|--|
| MambaAD (He et al., 2024) — Anomaly Scores | | | | | | | | | | | | | | | | | | |
| I-AUROC | | | | | | | | | | | | | | | | | | |
| I-AUROC | 0.842 | 0.928 | 0.798 | 0.780 | 0.875 | 0.793 | 0.701 | 0.868 | 0.891 | 0.902 | 0.871 | 0.857 | 0.880 | 0.697 | 0.980 | 0.944 | | |
| P-AUROC | 0.977 | 0.997 | 0.981 | 0.970 | 0.992 | 0.987 | 0.965 | 0.992 | 0.992 | 0.994 | 0.994 | 0.990 | 0.992 | 0.976 | 0.997 | 0.988 | | |
| P-AUPRO | 0.839 | 0.972 | 0.862 | 0.894 | 0.937 | 0.863 | 0.726 | 0.935 | 0.931 | 0.953 | 0.961 | 0.915 | 0.954 | 0.870 | 0.988 | 0.894 | | |
| Metric | switch | tape | t-block | t-brush | toy | t-brick | transistor1 | u-block | usb | u-adaptor | vcpill | w-beads | woodstick | zipper | Mean | | | |
| MambaAD (He et al., 2024) — Anomaly Scores | | | | | | | | | | | | | | | | | | |
| I-AUROC | | | | | | | | | | | | | | | | | | |
| I-AUROC | 0.917 | 0.968 | 0.961 | 0.851 | 0.830 | 0.705 | 0.944 | 0.897 | 0.920 | 0.794 | 0.883 | 0.825 | 0.804 | 0.992 | 0.863 | | | |
| P-AUROC | 0.982 | 0.998 | 0.998 | 0.975 | 0.960 | 0.966 | 0.994 | 0.995 | 0.992 | 0.973 | 0.987 | 0.980 | 0.977 | 0.993 | 0.985 | | | |
| P-AUPRO | 0.929 | 0.980 | 0.982 | 0.914 | 0.863 | 0.747 | 0.965 | 0.954 | 0.952 | 0.825 | 0.893 | 0.845 | 0.827 | 0.976 | 0.905 | | | |

prune false-positive noise, leading to more topologically precise anomaly segmentations as reflected in the superior F1 and Precision metrics.

 Table 13. Performance evaluation of Dinomaly (Guo et al., 2025) across 12 categories (VisA classes) and their mean, comparing three binary map strategies: (a) THR ($\mu + 3\sigma$), (b) TTT4AS, and (c) TopoOT. The table highlights the best result for each Precision, Recall, and F1 Score metric in **bold black** and the second-best in **blue**.

| Metric | candle | capsules | cashew | chewinggum | fryum | macaroni1 | macaroni2 | pcb1 | pcb2 | pcb3 | pcb4 | pipe_fryum | Mean |
|--|--------------|--------------|--------------|--------------|--------------|--------------|--------------|--------------|--------------|--------------|--------------|--------------|--------------|
| (a) Dinomaly - Binary Map - THR ($\mu + 3\sigma$) (Guo et al., 2025) | | | | | | | | | | | | | |
| | | | | | | | | | | | | | |
| Precision | 0.190 | 0.316 | 0.239 | 0.384 | 0.307 | 0.109 | 0.111 | 0.300 | 0.275 | 0.318 | 0.518 | 0.231 | 0.275 |
| Recall | 0.908 | 0.936 | 0.824 | 0.889 | 0.740 | 0.947 | 0.970 | 0.862 | 0.847 | 0.861 | 0.674 | 0.885 | 0.862 |
| F1 Score | 0.286 | 0.396 | 0.285 | 0.510 | 0.247 | 0.189 | 0.195 | 0.373 | 0.380 | 0.435 | 0.522 | 0.246 | 0.339 |
| IoU | 0.116 | 0.230 | 0.108 | 0.289 | 0.093 | 0.034 | 0.032 | 0.146 | 0.126 | 0.176 | 0.309 | 0.069 | 0.144 |
| (b) Dinomaly - Binary Map - TTT4AS (Costanzino et al., 2024a) | | | | | | | | | | | | | |
| | | | | | | | | | | | | | |
| Precision | 0.175 | 0.369 | 0.217 | 0.318 | 0.250 | 0.075 | 0.049 | 0.227 | 0.223 | 0.231 | 0.378 | 0.169 | 0.223 |
| Recall | 0.798 | 0.869 | 0.848 | 0.858 | 0.708 | 0.798 | 0.849 | 0.879 | 0.815 | 0.813 | 0.594 | 0.908 | 0.811 |
| F1 Score | 0.244 | 0.407 | 0.254 | 0.447 | 0.176 | 0.127 | 0.090 | 0.284 | 0.313 | 0.306 | 0.387 | 0.172 | 0.267 |
| IoU | 0.165 | 0.295 | 0.163 | 0.314 | 0.110 | 0.075 | 0.049 | 0.189 | 0.201 | 0.203 | 0.258 | 0.104 | 0.177 |
| (c) Dinomaly - Binary Map - TopoOT | | | | | | | | | | | | | |
| | | | | | | | | | | | | | |
| Precision | 0.398 | 0.613 | 0.459 | 0.650 | 0.490 | 0.395 | 0.363 | 0.661 | 0.649 | 0.642 | 0.738 | 0.498 | 0.546 |
| Recall | 0.658 | 0.553 | 0.676 | 0.648 | 0.467 | 0.569 | 0.573 | 0.505 | 0.468 | 0.458 | 0.371 | 0.695 | 0.553 |
| F1 Score | 0.410 | 0.497 | 0.448 | 0.584 | 0.329 | 0.432 | 0.420 | 0.532 | 0.515 | 0.501 | 0.428 | 0.470 | 0.464 |
| IoU | 0.175 | 0.298 | 0.177 | 0.388 | 0.129 | 0.115 | 0.097 | 0.275 | 0.268 | 0.285 | 0.329 | 0.134 | 0.223 |

Table 14. Dinomaly (Guo et al., 2025) on Real-IAD (30 classes). I-AUROC, P-AUROC, P-AUPRO.

| Metric | audiojack | b-cap | b-battery | e-cap | eraser | f-hood | mint | mounts | pcb | p-battery | p-nut | p-plug | p-doll | regulator | r-base | s-set | | |
|--|-----------|-------|-----------|---------|--------|---------|-------------|---------|-------|-----------|--------|---------|-----------|-----------|--------|-------|--|--|
| Dinomaly (Guo et al., 2025) — Anomaly Scores | | | | | | | | | | | | | | | | | | |
| | | | | | | | | | | | | | | | | | | |
| I-AUROC | 0.868 | 0.899 | 0.866 | 0.870 | 0.903 | 0.838 | 0.731 | 0.904 | 0.920 | 0.929 | 0.883 | 0.905 | 0.851 | 0.852 | 0.992 | 0.958 | | |
| P-AUROC | 0.917 | 0.981 | 0.929 | 0.960 | 0.964 | 0.930 | 0.776 | 0.956 | 0.957 | 0.968 | 0.974 | 0.964 | 0.960 | 0.956 | 0.985 | 0.909 | | |
| P-AUPRO | 0.917 | 0.981 | 0.929 | 0.960 | 0.964 | 0.930 | 0.776 | 0.956 | 0.957 | 0.968 | 0.974 | 0.964 | 0.960 | 0.956 | 0.985 | 0.909 | | |
| Metric | switch | tape | t-block | t-brush | toy | t-brick | transistor1 | u-block | usb | u-adaptor | vcpill | w-beads | woodstick | zipper | Mean | | | |
| Dinomaly (Guo et al., 2025) — Anomaly Scores | | | | | | | | | | | | | | | | | | |
| | | | | | | | | | | | | | | | | | | |
| I-AUROC | 0.978 | 0.969 | 0.967 | 0.904 | 0.856 | 0.723 | 0.974 | 0.899 | 0.920 | 0.815 | 0.920 | 0.873 | 0.840 | 0.991 | 0.893 | | | |
| P-AUROC | 0.959 | 0.988 | 0.988 | 0.904 | 0.910 | 0.766 | 0.978 | 0.968 | 0.975 | 0.910 | 0.937 | 0.905 | 0.904 | 0.978 | 0.989 | | | |
| P-AUPRO | 0.959 | 0.988 | 0.988 | 0.904 | 0.910 | 0.766 | 0.978 | 0.968 | 0.975 | 0.910 | 0.937 | 0.905 | 0.904 | 0.978 | 0.939 | | | |

Table 11 summarizes the performance of the Dinomaly architecture on the VisA dataset (12 classes) using standard evaluation metrics, including I-AUROC, P-AUROC, and P-AUPRO. To ensure a fair comparison and maintain empirical integrity, these baseline results were reproduced using the authors' official open-source implementation.

Table 12 details the evaluation of MambaAD across the 30 categories of the Real-IAD benchmark. Performance is reported in terms of I-AUROC, P-AUROC, and P-AUPRO, with all values derived directly from the official implementation to ensure

Table 15. Performance evaluation of MambaAD (He et al., 2024) across 30 classes (Real-IAD Dataset) and their mean, comparing three binary map strategies: (a) THR ($\mu + 3\sigma$), (b) TTT4AS, and (c) TopoOT. The best result for each Precision, Recall, and F1 Score is in **bold** and the second-best in **blue**.

| Metric | audiojack | b-cap | b-battery | e-cap | eraser | f-hood | mint | mounts | pcb | p-battery | p-nut | p-plug | p-doll | regulator | r-base | s-set |
|--|--------------|--------------|--------------|--------------|--------------|--------------|--------------|--------------|--------------|--------------|--------------|--------------|--------------|--------------|--------------|--------------|
| (a) MambaAD - Binary Map - THR ($\mu + 3\sigma$) (He et al., 2024) | | | | | | | | | | | | | | | | |
| | | | | | | | | | | | | | | | | |
| Precision | 0.164 | 0.055 | 0.199 | 0.202 | 0.121 | 0.126 | 0.082 | 0.209 | 0.438 | 0.178 | 0.132 | 0.101 | 0.122 | 0.074 | 0.144 | 0.156 |
| Recall | 0.510 | 0.944 | 0.333 | 0.475 | 0.648 | 0.514 | 0.385 | 0.759 | 0.472 | 0.815 | 0.783 | 0.846 | 0.794 | 0.548 | 0.950 | 0.743 |
| F1 Score | 0.210 | 0.100 | 0.160 | 0.181 | 0.188 | 0.178 | 0.120 | 0.254 | 0.309 | 0.280 | 0.202 | 0.173 | 0.189 | 0.107 | 0.227 | 0.245 |
| IoU | 0.133 | 0.055 | 0.102 | 0.116 | 0.114 | 0.112 | 0.076 | 0.162 | 0.212 | 0.171 | 0.124 | 0.100 | 0.114 | 0.062 | 0.139 | 0.155 |
| (b) MambaAD - Binary Map - TTT4AS (Costanzino et al., 2024a) | | | | | | | | | | | | | | | | |
| Precision | 0.062 | 0.027 | 0.075 | 0.039 | 0.059 | 0.051 | 0.046 | 0.097 | 0.075 | 0.084 | 0.055 | 0.048 | 0.073 | 0.034 | 0.071 | 0.091 |
| Recall | 0.605 | 0.953 | 0.629 | 0.684 | 0.739 | 0.692 | 0.461 | 0.833 | 0.870 | 0.887 | 0.799 | 0.870 | 0.830 | 0.534 | 0.951 | 0.762 |
| F1 Score | 0.109 | 0.052 | 0.108 | 0.072 | 0.105 | 0.090 | 0.075 | 0.164 | 0.135 | 0.151 | 0.099 | 0.089 | 0.124 | 0.061 | 0.127 | 0.154 |
| IoU | 0.062 | 0.027 | 0.066 | 0.039 | 0.059 | 0.050 | 0.044 | 0.097 | 0.074 | 0.084 | 0.055 | 0.048 | 0.071 | 0.034 | 0.071 | 0.091 |
| (c) MambaAD - Binary Map - TopoOT | | | | | | | | | | | | | | | | |
| Precision | 0.239 | 0.245 | 0.164 | 0.156 | 0.254 | 0.183 | 0.133 | 0.422 | 0.297 | 0.404 | 0.269 | 0.229 | 0.324 | 0.171 | 0.411 | 0.398 |
| Recall | 0.491 | 0.829 | 0.513 | 0.612 | 0.585 | 0.544 | 0.355 | 0.637 | 0.745 | 0.679 | 0.695 | 0.766 | 0.584 | 0.451 | 0.803 | 0.629 |
| F1 Score | 0.284 | 0.347 | 0.169 | 0.225 | 0.303 | 0.233 | 0.155 | 0.444 | 0.367 | 0.435 | 0.341 | 0.317 | 0.365 | 0.203 | 0.465 | 0.430 |
| IoU | 0.197 | 0.231 | 0.106 | 0.143 | 0.203 | 0.159 | 0.102 | 0.324 | 0.255 | 0.317 | 0.236 | 0.206 | 0.246 | 0.139 | 0.342 | 0.322 |
| Metric | switch | tape | t-block | t-brush | toy | t-brick | transistor | 1 | u-block | usb | u-adaptor | vepill | w-beads | woodstick | zipper | Mean |
| (a) MambaAD - Binary Map - THR ($\mu + 3\sigma$) (He et al., 2024) | | | | | | | | | | | | | | | | |
| Precision | 0.252 | 0.129 | 0.165 | 0.396 | 0.149 | 0.264 | 0.218 | 0.131 | 0.289 | 0.053 | 0.331 | 0.194 | 0.188 | 0.378 | 0.188 | |
| Recall | 0.736 | 0.953 | 0.951 | 0.442 | 0.535 | 0.268 | 0.729 | 0.794 | 0.699 | 0.586 | 0.598 | 0.429 | 0.540 | 0.805 | 0.653 | |
| F1 Score | 0.331 | 0.214 | 0.265 | 0.309 | 0.188 | 0.213 | 0.316 | 0.211 | 0.320 | 0.090 | 0.380 | 0.227 | 0.242 | 0.399 | 0.228 | |
| IoU | 0.226 | 0.128 | 0.161 | 0.203 | 0.118 | 0.148 | 0.200 | 0.130 | 0.211 | 0.050 | 0.270 | 0.148 | 0.155 | 0.269 | 0.145 | |
| (b) MambaAD - Binary Map - TTT4AS (Costanzino et al., 2024a) | | | | | | | | | | | | | | | | |
| Precision | 0.123 | 0.085 | 0.063 | 0.246 | 0.053 | 0.078 | 0.120 | 0.071 | 0.086 | 0.024 | 0.169 | 0.099 | 0.085 | 0.221 | 0.084 | |
| Recall | 0.856 | 0.956 | 0.989 | 0.624 | 0.636 | 0.585 | 0.893 | 0.838 | 0.907 | 0.577 | 0.741 | 0.626 | 0.668 | 0.905 | 0.763 | |
| F1 Score | 0.200 | 0.149 | 0.116 | 0.299 | 0.093 | 0.131 | 0.205 | 0.125 | 0.153 | 0.045 | 0.258 | 0.159 | 0.146 | 0.310 | 0.137 | |
| IoU | 0.122 | 0.084 | 0.063 | 0.194 | 0.052 | 0.077 | 0.119 | 0.071 | 0.086 | 0.023 | 0.163 | 0.096 | 0.084 | 0.204 | 0.080 | |
| (c) MambaAD - Binary Map - TopoOT | | | | | | | | | | | | | | | | |
| Precision | 0.430 | 0.404 | 0.423 | 0.454 | 0.222 | 0.189 | 0.348 | 0.338 | 0.370 | 0.127 | 0.481 | 0.263 | 0.258 | 0.535 | 0.305 | |
| Recall | 0.661 | 0.747 | 0.866 | 0.409 | 0.594 | 0.510 | 0.573 | 0.721 | 0.736 | 0.572 | 0.510 | 0.476 | 0.521 | 0.665 | 0.616 | |
| F1 Score | 0.455 | 0.460 | 0.520 | 0.368 | 0.292 | 0.235 | 0.385 | 0.412 | 0.440 | 0.179 | 0.430 | 0.296 | 0.318 | 0.520 | 0.346 | |
| IoU | 0.330 | 0.322 | 0.378 | 0.247 | 0.205 | 0.159 | 0.267 | 0.295 | 0.317 | 0.117 | 0.311 | 0.208 | 0.221 | 0.378 | 0.243 | |

consistency with reported state-of-the-art benchmarks.

We evaluate the effectiveness of **TopoOT** against competing binary mapping strategies on the Dinomaly backbone (Table 13). TopoOT consistently secures the highest F1 Score and Precision across the 12 VisA categories. Notably, our method achieves a mean F1 Score of **0.464**, outperforming THR and TTT4AS by **+0.125** and **+0.197**, respectively. Precision scores exhibit even more significant growth, with improvements of **+0.271** (vs. THR) and **+0.323** (vs. TTT4AS). These results underscore the generalizability of our approach, establishing TopoOT as a state-of-the-art technique for refined anomaly detection.

Table 14 details the performance of the Dinomaly framework across the 30 categories of the Real-IAD benchmark. Anomaly detection and segmentation efficacy are quantified using standard metrics, including I-AUROC, P-AUROC, and P-AUPRO. To ensure a standardized baseline for comparison, all results were reproduced using the authors' official open-source implementation, maintaining consistency with reported state-of-the-art values.

In Table 15, **TopoOT** demonstrates superior performance when integrated with the MambaAD architecture on the Real-IAD dataset. Across 30 distinct classes, TopoOT consistently yields the highest scores in most evaluation categories. Notably, it improves the average F1 Score by **+0.058** (vs. THR) and **+0.209** (vs. TTT4AS). Precision metrics follow a similar trajectory, with gains of **+0.117** and **+0.221** over the respective baselines. The consistency of these gains underscores TopoOT's effectiveness as a robust post-processing paradigm for complex, multi-class anomaly detection scenarios.

The quantitative evaluation in Table 16 reveals that TopoOT consistently outperforms existing binarization frameworks on the Dinomaly backbone. By securing the top rank in F1 Score and Precision across the majority of categories, our method establishes a new performance baseline. Specifically, TopoOT reaches a mean F1 Score of 0.442, representing a substantial margin of +0.125 over THR and +0.213 over TTT4AS. These improvements are mirrored in Precision, where TopoOT (0.461) exceeds the baselines by +0.219 and +0.307, respectively. Such consistent gains validate the efficacy of topology-aware optimization in refining complex anomaly segmentations during test-time adaptation.

Table 16. Performance evaluation of Dinomaly (Guo et al., 2025) across 30 classes (Real-IAD Dataset) and their mean, comparing three binary map strategies: (a) THR ($\mu + 3\sigma$), (b) TTT4AS, and (c) TopoOT. The best result for each Precision, Recall, and F1 Score is in **bold** and the second-best in **blue**.

| Metric | audiojack | b-cap | b-battery | e-cap | eraser | f-hood | mint | mounts | pcb | p-battery | p-nut | p-plug | p-doll | regulator | r-base | s-set |
|--|--------------|--------------|--------------|--------------|--------------|--------------|--------------|--------------|--------------|--------------|--------------|--------------|--------------|--------------|--------------|--------------|
| (a) Dinomaly - Binary Map - THR ($\mu + 3\sigma$) (Guo et al., 2025) | | | | | | | | | | | | | | | | |
| | | | | | | | | | | | | | | | | |
| Precision | 0.366 | 0.105 | 0.274 | 0.304 | 0.164 | 0.196 | 0.144 | 0.222 | 0.383 | 0.186 | 0.159 | 0.134 | 0.193 | 0.132 | 0.170 | 0.184 |
| Recall | 0.645 | 0.985 | 0.435 | 0.663 | 0.832 | 0.775 | 0.664 | 0.826 | 0.719 | 0.903 | 0.885 | 0.937 | 0.737 | 0.895 | 0.996 | 0.776 |
| F1 Score | 0.427 | 0.186 | 0.282 | 0.350 | 0.260 | 0.290 | 0.217 | 0.325 | 0.442 | 0.299 | 0.259 | 0.229 | 0.273 | 0.215 | 0.272 | 0.279 |
| IoU | 0.303 | 0.105 | 0.187 | 0.234 | 0.163 | 0.183 | 0.138 | 0.217 | 0.312 | 0.185 | 0.158 | 0.133 | 0.172 | 0.130 | 0.169 | 0.183 |
| (b) Dinomaly - Binary Map - TTT4AS (Costanzino et al., 2024a) | | | | | | | | | | | | | | | | |
| | | | | | | | | | | | | | | | | |
| Precision | 0.102 | 0.056 | 0.113 | 0.093 | 0.107 | 0.098 | 0.095 | 0.229 | 0.184 | 0.188 | 0.122 | 0.102 | 0.123 | 0.121 | 0.184 | 0.174 |
| Recall | 0.804 | 0.721 | 0.504 | 0.874 | 0.803 | 0.807 | 0.532 | 0.888 | 0.844 | 0.866 | 0.866 | 0.904 | 0.730 | 0.816 | 0.924 | 0.720 |
| F1 Score | 0.171 | 0.098 | 0.135 | 0.159 | 0.169 | 0.159 | 0.145 | 0.328 | 0.281 | 0.297 | 0.198 | 0.176 | 0.177 | 0.188 | 0.285 | 0.263 |
| IoU | 0.103 | 0.056 | 0.091 | 0.093 | 0.107 | 0.098 | 0.094 | 0.224 | 0.183 | 0.187 | 0.123 | 0.102 | 0.112 | 0.121 | 0.182 | 0.175 |
| (c) Dinomaly - Binary Map - TopoOT | | | | | | | | | | | | | | | | |
| | | | | | | | | | | | | | | | | |
| Precision | 0.465 | 0.383 | 0.333 | 0.339 | 0.418 | 0.360 | 0.307 | 0.559 | 0.526 | 0.562 | 0.368 | 0.399 | 0.406 | 0.445 | 0.583 | 0.475 |
| Recall | 0.604 | 0.662 | 0.415 | 0.653 | 0.579 | 0.660 | 0.501 | 0.505 | 0.606 | 0.561 | 0.609 | 0.711 | 0.562 | 0.505 | 0.699 | 0.477 |
| F1 Score | 0.465 | 0.460 | 0.259 | 0.400 | 0.441 | 0.410 | 0.308 | 0.490 | 0.529 | 0.515 | 0.388 | 0.465 | 0.409 | 0.436 | 0.581 | 0.382 |
| IoU | 0.335 | 0.320 | 0.162 | 0.275 | 0.315 | 0.294 | 0.211 | 0.369 | 0.390 | 0.380 | 0.273 | 0.328 | 0.287 | 0.315 | 0.439 | 0.275 |
| Metric | switch | tape | t-block | t-brush | toy | t-brick | transistor | 1u-block | usb | u-adaptor | vcpill | w-beads | woodstick | zipper | Mean | |
| (a) Dinomaly - Binary Map - THR ($\mu + 3\sigma$) (Guo et al., 2025) | | | | | | | | | | | | | | | | |
| | | | | | | | | | | | | | | | | |
| Precision | 0.336 | 0.190 | 0.182 | 0.427 | 0.174 | 0.310 | 0.312 | 0.190 | 0.323 | 0.094 | 0.452 | 0.310 | 0.206 | 0.452 | 0.242 | |
| Recall | 0.931 | 0.973 | 0.967 | 0.374 | 0.647 | 0.654 | 0.884 | 0.836 | 0.874 | 0.923 | 0.740 | 0.721 | 0.831 | 0.747 | 0.793 | |
| F1 Score | 0.467 | 0.301 | 0.296 | 0.307 | 0.219 | 0.348 | 0.438 | 0.286 | 0.431 | 0.165 | 0.499 | 0.393 | 0.310 | 0.431 | 0.317 | |
| IoU | 0.324 | 0.189 | 0.180 | 0.205 | 0.133 | 0.236 | 0.292 | 0.187 | 0.288 | 0.094 | 0.367 | 0.271 | 0.199 | 0.293 | 0.208 | |
| (b) Dinomaly - Binary Map - TTT4AS (Costanzino et al., 2024a) | | | | | | | | | | | | | | | | |
| | | | | | | | | | | | | | | | | |
| Precision | 0.154 | 0.150 | 0.160 | 0.312 | 0.109 | 0.153 | 0.200 | 0.121 | 0.159 | 0.052 | 0.296 | 0.161 | 0.154 | 0.351 | 0.154 | |
| Recall | 0.927 | 0.928 | 0.951 | 0.553 | 0.625 | 0.860 | 0.812 | 0.794 | 0.882 | 0.702 | 0.871 | 0.838 | 0.878 | 0.815 | 0.801 | |
| F1 Score | 0.233 | 0.240 | 0.260 | 0.342 | 0.166 | 0.236 | 0.295 | 0.192 | 0.245 | 0.087 | 0.410 | 0.250 | 0.245 | 0.430 | 0.229 | |
| IoU | 0.148 | 0.151 | 0.159 | 0.233 | 0.105 | 0.151 | 0.187 | 0.121 | 0.155 | 0.052 | 0.292 | 0.160 | 0.153 | 0.298 | 0.147 | |
| (c) Dinomaly - Binary Map - TopoOT | | | | | | | | | | | | | | | | |
| | | | | | | | | | | | | | | | | |
| Precision | 0.629 | 0.434 | 0.632 | 0.526 | 0.382 | 0.395 | 0.579 | 0.443 | 0.515 | 0.325 | 0.627 | 0.458 | 0.302 | 0.641 | 0.461 | |
| Recall | 0.526 | 0.626 | 0.722 | 0.274 | 0.504 | 0.670 | 0.513 | 0.607 | 0.608 | 0.566 | 0.574 | 0.606 | 0.703 | 0.506 | 0.577 | |
| F1 Score | 0.527 | 0.429 | 0.636 | 0.294 | 0.380 | 0.430 | 0.500 | 0.452 | 0.520 | 0.352 | 0.540 | 0.458 | 0.340 | 0.466 | 0.442 | |
| IoU | 0.374 | 0.300 | 0.490 | 0.191 | 0.275 | 0.301 | 0.352 | 0.331 | 0.372 | 0.234 | 0.402 | 0.337 | 0.239 | 0.330 | 0.317 | |

A.5. Additional Quantitative Results on 3D AD&S Datasets

Table 17 provides a comprehensive performance analysis of the CMM framework on the MVTec 3D-AD benchmark. Anomaly detection and segmentation efficacy are quantified via standard metrics, including I-AUROC, P-AUROC, and P-AUPRO. To ensure empirical integrity and a standardized baseline for comparison, all results were reproduced using the authors' official open-source implementation.

The performance of M3DM on the MVTec 3D-AD dataset is summarized in Table 18, with scores reported across I-AUROC, P-AUROC, and P-AUPRO metrics. All values were derived directly from the official implementation to maintain fidelity with the reported state-of-the-art benchmarks.

Table 17. CMM (Costanzino et al., 2024b) anomaly scores across categories of the MVTec 3D-AD dataset (Bergmann et al., 2021b).

| Metric | Bagel | Gland | Carrot | Cookie | Dowel | Foam | Peach | Potato | Rope | Tire | Mean |
|--|-------|-------|--------|--------|-------|-------|-------|--------|-------|-------|-------|
| CMM (Costanzino et al., 2024b) – Anomaly Score | | | | | | | | | | | |
| I-AUROC | 0.994 | 0.888 | 0.984 | 0.993 | 0.980 | 0.888 | 0.941 | 0.943 | 0.980 | 0.953 | 0.954 |
| P-AUROC | 0.997 | 0.992 | 0.999 | 0.972 | 0.987 | 0.993 | 0.998 | 0.999 | 0.998 | 0.998 | 0.993 |
| P-AUPRO | 0.979 | 0.972 | 0.982 | 0.945 | 0.950 | 0.968 | 0.980 | 0.982 | 0.975 | 0.981 | 0.971 |

Table 19 provides a quantitative evaluation of our proposed method, TopoOT, against the THR and TTT4AS baselines using the CMM backbone on MVTec 3D-AD. Mean performance metrics reveal that TopoOT consistently surpasses both baselines across most criteria. In terms of Precision, TopoOT achieves a mean of 0.427, substantially improving over THR (0.199) and TTT4AS (0.303). While THR yields a higher Recall (0.902), it suffers from significant over-segmentation; TopoOT maintains a more effective Recall of 0.845, outperforming TTT4AS (0.608).

The efficacy of our approach is most evident in the F1 Score and IoU metrics. TopoOT secures a mean F1 Score of 0.482, marking significant gains of +0.207 over THR and +0.102 over TTT4AS. Similarly, our method obtains a mean IoU of 0.343, demonstrating a clear margin over THR (0.232) and a major improvement over TTT4AS (0.077).

These gains are particularly pronounced in categories such as Gland, Cookie, and Carrot. While the THR baseline exhibits high sensitivity, its poor Precision indicates a lack of specificity. In contrast, TopoOT provides a superior balance between sensitivity and specificity, yielding robust anomaly localization. Overall, these results confirm that TopoOT generalizes effectively across diverse 3D geometries, establishing a state-of-the-art paradigm for topology-aware test-time adaptation.

Table 18. M3DM (Wang et al., 2023) anomaly scores across categories of the MVTec 3D-AD dataset (Bergmann et al., 2021b).

| Metric | Bagel | Gland | Carrot | Cookie | Dowel | Foam | Peach | Potato | Rope | Tire | Mean |
|--|-------|-------|--------|--------|-------|-------|-------|--------|-------|-------|-------|
| M3DM (Wang et al., 2023) – Anomaly Score | | | | | | | | | | | |
| I-AUROC | 0.994 | 0.909 | 0.972 | 0.976 | 0.960 | 0.942 | 0.973 | 0.899 | 0.972 | 0.850 | 0.945 |
| P-AUROC | 0.995 | 0.993 | 0.997 | 0.985 | 0.985 | 0.984 | 0.996 | 0.994 | 0.997 | 0.996 | 0.992 |
| P-AUPRO | 0.970 | 0.971 | 0.979 | 0.950 | 0.941 | 0.932 | 0.977 | 0.971 | 0.971 | 0.975 | 0.964 |

Table 19. Evaluation of CMM (Costanzino et al., 2024b) across benchmarks in the MVTec 3D-AD (Bergmann et al., 2021b).

| Method | Bagel | Gland | Carrot | Cookie | Dowel | Foam | Peach | Potato | Rope | Tire | Mean |
|---|--------------|--------------|--------------|--------------|--------------|--------------|--------------|--------------|--------------|--------------|--------------|
| (a) CMM - Binary Map - THR ($\mu + 3\sigma$) (Costanzino et al., 2024b) | | | | | | | | | | | |
| Precision | 0.301 | 0.188 | 0.049 | 0.518 | 0.072 | 0.275 | 0.262 | 0.092 | 0.049 | 0.182 | 0.199 |
| Recall | 0.949 | 0.842 | 0.998 | 0.901 | 0.896 | 0.597 | 0.957 | 0.998 | 0.989 | 0.896 | 0.902 |
| F1 Score | 0.425 | 0.265 | 0.092 | 0.619 | 0.129 | 0.327 | 0.375 | 0.160 | 0.091 | 0.267 | 0.275 |
| IoU | 0.411 | 0.182 | 0.102 | 0.578 | 0.105 | 0.276 | 0.233 | 0.085 | 0.149 | 0.198 | 0.232 |
| (b) CMM - Binary Map - TTT4AS (Costanzino et al., 2024a) | | | | | | | | | | | |
| Precision | 0.432 | 0.258 | 0.242 | 0.713 | 0.195 | 0.214 | 0.353 | 0.252 | 0.264 | 0.111 | 0.303 |
| Recall | 0.745 | 0.766 | 0.889 | 0.603 | 0.739 | 0.732 | 0.872 | 0.888 | 0.865 | 0.904 | 0.800 |
| F1 Score | 0.495 | 0.362 | 0.351 | 0.606 | 0.289 | 0.311 | 0.470 | 0.363 | 0.360 | 0.189 | 0.380 |
| IoU | 0.264 | 0.037 | 0.029 | 0.231 | 0.031 | 0.058 | 0.034 | 0.028 | 0.029 | 0.030 | 0.077 |
| (c) CMM - Binary Map - TopoOT | | | | | | | | | | | |
| Precision | 0.560 | 0.347 | 0.398 | 0.841 | 0.387 | 0.298 | 0.432 | 0.308 | 0.477 | 0.224 | 0.427 |
| Recall | 0.847 | 0.849 | 0.905 | 0.643 | 0.658 | 0.893 | 0.903 | 0.947 | 0.822 | 0.980 | 0.845 |
| F1 Score | 0.618 | 0.419 | 0.516 | 0.672 | 0.438 | 0.345 | 0.519 | 0.411 | 0.525 | 0.360 | 0.482 |
| IoU | 0.476 | 0.305 | 0.371 | 0.535 | 0.312 | 0.238 | 0.387 | 0.289 | 0.394 | 0.119 | 0.343 |

Table 20 evaluates TopoOT against THR and TTT4AS using the M3DM backbone on MVTec 3D-AD. TopoOT consistently improves nearly all metrics, achieving a mean Precision of 0.564 (+0.391 over THR; +0.097 over TTT4AS). While THR shows higher Recall (0.889) due to over-segmentation, TopoOT provides a more balanced 0.767 Recall, significantly outperforming TTT4AS (0.640).

The method's efficacy is clearest in the F1 Score (0.490) and IoU (0.364), yielding gains of up to +0.245 and +0.244 over baselines, respectively. These results confirm TopoOT's superior generalization across diverse 3D anomaly scenarios.

Table 20. Evaluation of M3DM (Wang et al., 2023) across benchmarks in the MVTec 3D-AD (Bergmann et al., 2021b).

| Method | Bagel | Gland | Carrot | Cookie | Dowel | Foam | Peach | Potato | Rope | Tire | Mean |
|---|--------------|--------------|--------------|--------------|--------------|--------------|--------------|--------------|--------------|--------------|--------------|
| (a) M3DM - Binary Map - THR ($\mu + 3\sigma$) (Wang et al., 2023) | | | | | | | | | | | |
| Precision | 0.174 | 0.105 | 0.045 | 0.493 | 0.221 | 0.254 | 0.067 | 0.050 | 0.194 | 0.127 | 0.173 |
| Recall | 0.949 | 0.980 | 0.997 | 0.712 | 0.909 | 0.536 | 1.000 | 0.999 | 0.917 | 0.894 | 0.889 |
| F1 Score | 0.270 | 0.174 | 0.085 | 0.547 | 0.328 | 0.318 | 0.121 | 0.094 | 0.308 | 0.204 | 0.245 |
| IoU | 0.431 | 0.189 | 0.114 | 0.552 | 0.151 | 0.333 | 0.198 | 0.117 | 0.182 | 0.053 | 0.232 |
| (b) M3DM - Binary Map - TTT4AS (Costanzino et al., 2024a) | | | | | | | | | | | |
| Precision | 0.498 | 0.486 | 0.337 | 0.752 | 0.464 | 0.386 | 0.536 | 0.347 | 0.561 | 0.302 | 0.467 |
| Recall | 0.607 | 0.706 | 0.750 | 0.351 | 0.691 | 0.624 | 0.779 | 0.684 | 0.543 | 0.669 | 0.640 |
| F1 Score | 0.478 | 0.525 | 0.422 | 0.443 | 0.514 | 0.440 | 0.585 | 0.419 | 0.468 | 0.383 | 0.468 |
| IoU | 0.287 | 0.078 | 0.031 | 0.343 | 0.066 | 0.148 | 0.090 | 0.026 | 0.099 | 0.028 | 0.120 |
| (c) M3DM - Binary Map - TopoOT | | | | | | | | | | | |
| Precision | 0.870 | 0.357 | 0.490 | 0.829 | 0.566 | 0.379 | 0.603 | 0.490 | 0.254 | 0.798 | 0.564 |
| Recall | 0.744 | 0.806 | 0.794 | 0.571 | 0.685 | 0.910 | 0.862 | 0.823 | 0.540 | 0.935 | 0.767 |
| F1 Score | 0.655 | 0.406 | 0.559 | 0.626 | 0.564 | 0.452 | 0.661 | 0.541 | 0.304 | 0.127 | 0.490 |
| IoU | 0.515 | 0.294 | 0.406 | 0.480 | 0.418 | 0.333 | 0.519 | 0.401 | 0.195 | 0.077 | 0.364 |

 Table 21. Performance evaluation of PO3AD (Ye et al., 2025) across 29 categories of Anomaly-ShapeNet (Li et al., 2024) and their mean, comparing three binary map strategies: (a) THR ($\mu + 3\sigma$), (b) TTT4AS, and (c) TopoOT. The table highlights the best result for each Precision, Recall, and F1 Score metric in **bold black** and the second-best in **blue**.

| Metric | ashtray0 | bag0 | bottle0 | bottle1 | bottle3 | bowl0 | bowl1 | bowl2 | bowl3 | bowl4 | bowl5 | bucket0 | bucket1 | cap0 | cap3 |
|--|--------------|--------------|--------------|--------------|--------------|--------------|--------------|--------------|--------------|--------------|--------------|--------------|--------------|--------------|--------------|
| (a) PO3AD — Binary Map — THR ($\mu + 3\sigma$) (Ye et al., 2025) | | | | | | | | | | | | | | | |
| Precision | 0.920 | 0.678 | 0.737 | 0.714 | 0.847 | 0.797 | 0.589 | 0.815 | 0.607 | 0.872 | 0.647 | 0.709 | 0.716 | 0.781 | 0.726 |
| Recall | 0.280 | 0.362 | 0.346 | 0.326 | 0.637 | 0.301 | 0.702 | 0.639 | 0.707 | 0.746 | 0.472 | 0.256 | 0.284 | 0.275 | 0.527 |
| F1 Score | 0.417 | 0.464 | 0.460 | 0.420 | 0.720 | 0.429 | 0.630 | 0.713 | 0.644 | 0.793 | 0.539 | 0.359 | 0.387 | 0.390 | 0.720 |
| IoU | 0.272 | 0.344 | 0.331 | 0.285 | 0.586 | 0.278 | 0.482 | 0.596 | 0.496 | 0.660 | 0.410 | 0.236 | 0.263 | 0.255 | 0.487 |
| (b) PO3AD — Binary Map — TTT4AS (Costanzino et al., 2024a) | | | | | | | | | | | | | | | |
| Precision | 0.581 | 0.492 | 0.623 | 0.601 | 0.688 | 0.654 | 0.489 | 0.677 | 0.503 | 0.712 | 0.551 | 0.599 | 0.611 | 0.635 | 0.618 |
| Recall | 0.452 | 0.510 | 0.411 | 0.405 | 0.595 | 0.388 | 0.615 | 0.559 | 0.621 | 0.646 | 0.503 | 0.354 | 0.381 | 0.370 | 0.501 |
| F1 Score | 0.508 | 0.501 | 0.495 | 0.484 | 0.638 | 0.487 | 0.545 | 0.612 | 0.556 | 0.677 | 0.526 | 0.444 | 0.469 | 0.467 | 0.553 |
| IoU | 0.341 | 0.334 | 0.329 | 0.319 | 0.469 | 0.322 | 0.375 | 0.441 | 0.385 | 0.512 | 0.357 | 0.286 | 0.306 | 0.305 | 0.383 |
| (c) PO3AD — Binary Map — TopoOT | | | | | | | | | | | | | | | |
| Precision | 0.849 | 0.598 | 0.707 | 0.672 | 0.804 | 0.768 | 0.568 | 0.789 | 0.576 | 0.831 | 0.619 | 0.696 | 0.701 | 0.726 | 0.706 |
| Recall | 0.463 | 0.421 | 0.411 | 0.411 | 0.722 | 0.395 | 0.740 | 0.687 | 0.764 | 0.798 | 0.538 | 0.382 | 0.439 | 0.463 | 0.530 |
| F1 Score | 0.545 | 0.453 | 0.484 | 0.470 | 0.748 | 0.512 | 0.633 | 0.726 | 0.629 | 0.801 | 0.562 | 0.430 | 0.433 | 0.525 | 0.592 |
| IoU | 0.402 | 0.343 | 0.355 | 0.337 | 0.625 | 0.354 | 0.483 | 0.615 | 0.483 | 0.670 | 0.435 | 0.299 | 0.303 | 0.390 | 0.473 |
| Metric | cup0 | cup1 | eraser0 | headset0 | headset1 | helmet0 | helmet1 | vase1 | vase2 | vase3 | vase4 | vase7 | vase8 | vase9 | Mean |
| (a) PO3AD — Binary Map — THR ($\mu + 3\sigma$) (Ye et al., 2025) | | | | | | | | | | | | | | | |
| Precision | 0.782 | 0.524 | 0.801 | 0.649 | 0.697 | 0.239 | 0.513 | 0.404 | 0.600 | 0.572 | 0.468 | 0.627 | 0.777 | 0.777 | 0.675 |
| Recall | 0.443 | 0.326 | 0.314 | 0.339 | 0.302 | 0.215 | 0.370 | 0.336 | 0.486 | 0.292 | 0.584 | 0.733 | 0.605 | 0.572 | 0.441 |
| F1 Score | 0.558 | 0.389 | 0.436 | 0.431 | 0.411 | 0.216 | 0.411 | 0.356 | 0.520 | 0.351 | 0.503 | 0.663 | 0.663 | 0.627 | 0.500 |
| IoU | 0.401 | 0.276 | 0.301 | 0.293 | 0.269 | 0.132 | 0.276 | 0.259 | 0.383 | 0.245 | 0.383 | 0.502 | 0.562 | 0.511 | 0.371 |
| (b) PO3AD — Binary Map — TTT4AS (Costanzino et al., 2024a) | | | | | | | | | | | | | | | |
| Precision | 0.641 | 0.445 | 0.672 | 0.540 | 0.589 | 0.198 | 0.415 | 0.355 | 0.511 | 0.498 | 0.417 | 0.533 | 0.655 | 0.661 | 0.562 |
| Recall | 0.512 | 0.455 | 0.389 | 0.458 | 0.399 | 0.311 | 0.544 | 0.410 | 0.501 | 0.321 | 0.540 | 0.588 | 0.619 | 0.582 | 0.485 |
| F1 Score | 0.569 | 0.450 | 0.493 | 0.496 | 0.476 | 0.242 | 0.471 | 0.381 | 0.506 | 0.390 | 0.470 | 0.559 | 0.637 | 0.619 | 0.510 |
| IoU | 0.398 | 0.290 | 0.327 | 0.329 | 0.312 | 0.138 | 0.308 | 0.235 | 0.339 | 0.242 | 0.307 | 0.388 | 0.467 | 0.448 | 0.347 |
| (c) PO3AD — Binary Map — TopoOT | | | | | | | | | | | | | | | |
| Precision | 0.746 | 0.446 | 0.783 | 0.571 | 0.666 | 0.156 | 0.318 | 0.364 | 0.548 | 0.566 | 0.432 | 0.603 | 0.745 | 0.733 | 0.631 |
| Recall | 0.549 | 0.571 | 0.368 | 0.543 | 0.370 | 0.444 | 0.666 | 0.460 | 0.523 | 0.349 | 0.622 | 0.646 | 0.723 | 0.659 | 0.540 |
| F1 Score | 0.613 | 0.426 | 0.478 | 0.486 | 0.449 | 0.223 | 0.388 | 0.360 | 0.518 | 0.387 | 0.489 | 0.611 | 0.697 | 0.666 | 0.529 |
| IoU | 0.468 | 0.310 | 0.342 | 0.353 | 0.300 | 0.135 | 0.259 | 0.255 | 0.377 | 0.278 | 0.371 | 0.465 | 0.612 | 0.559 | 0.402 |

Table 22. PO3AD (Ye et al., 2025) — Anomaly scores, Object-AUROC, Point-AUROC, Object-AUCPR.

| Metric | ashtray0 bag0 bottle0 bottle1 bottle3 bowl0 bowl1 bowl2 bowl3 bowl4 bowl5 bucket0 bucket1 cap0 cap3 | | | | | | | | | | | | | | | | |
|--|---|-------|-------|-------|-------|-------|-------|-------|-------|-------|-------|-------|-------|-------|-------|--|--|
| PO3AD (Ye et al., 2025) — Anomaly Scores | | | | | | | | | | | | | | | | | |
| O-AUROC | 1.000 | 0.833 | 0.900 | 0.933 | 0.926 | 0.922 | 0.829 | 0.833 | 0.881 | 0.981 | 0.849 | 0.853 | 0.787 | 0.877 | 0.859 | | |
| P-AUROC | 0.962 | 0.949 | 0.912 | 0.844 | 0.880 | 0.978 | 0.914 | 0.918 | 0.935 | 0.967 | 0.941 | 0.755 | 0.899 | 0.957 | 0.948 | | |
| O-AUCPR | 0.999 | 0.809 | 0.927 | 0.959 | 0.962 | 0.946 | 0.905 | 0.888 | 0.927 | 0.985 | 0.904 | 0.923 | 0.882 | 0.841 | 0.906 | | |
| Metric | cup0 cup1 eraser0 headset0 headset1 helmet0 helmet1 vase1 vase2 vase3 vase4 vase7 vase8 vase9 Mean | | | | | | | | | | | | | | | | |
| PO3AD (Ye et al., 2025) — Anomaly Scores | | | | | | | | | | | | | | | | | |
| O-AUROC | 0.871 | 0.833 | 0.995 | 0.808 | 0.923 | 0.762 | 0.961 | 0.742 | 0.952 | 0.821 | 0.675 | 0.966 | 0.739 | 0.830 | 0.867 | | |
| P-AUROC | 0.909 | 0.932 | 0.974 | 0.823 | 0.907 | 0.878 | 0.948 | 0.882 | 0.978 | 0.884 | 0.902 | 0.982 | 0.950 | 0.952 | 0.919 | | |
| O-AUCPR | 0.879 | 0.870 | 0.995 | 0.765 | 0.914 | 0.864 | 0.961 | 0.789 | 0.963 | 0.902 | 0.824 | 0.971 | 0.833 | 0.904 | 0.903 | | |

Table 21 evaluates the performance of TopoOT against the THR and TTT4AS baselines using the PO3AD backbone on the Anomaly-ShapeNet dataset. The results indicate that TopoOT consistently outperforms both baselines across all reported metrics. Specifically, TopoOT achieves significant mean gains of +0.099 in Recall, +0.029 in F1 Score, and +0.031 in IoU relative to THR.

The improvements over TTT4AS are even more pronounced, with TopoOT exceeding it by +0.069 in Precision, +0.055 in Recall, and +0.019 in F1 Score. These results, supported by strong performance across individual categories, demonstrate that TopoOT establishes a new state-of-the-art while generalizing robustly across diverse anomaly types. This consistent success across different backbones further validates the effectiveness of our topology-aware optimization.

Table 22 provides the benchmark performance of the PO3AD framework on the Anomaly-ShapeNet dataset. Anomaly detection efficacy is quantified via Object-AUROC, Point-AUROC, and Object-AUCPR metrics. To ensure empirical integrity and a standardized baseline for comparison, these results were reproduced using the authors’ official open-source

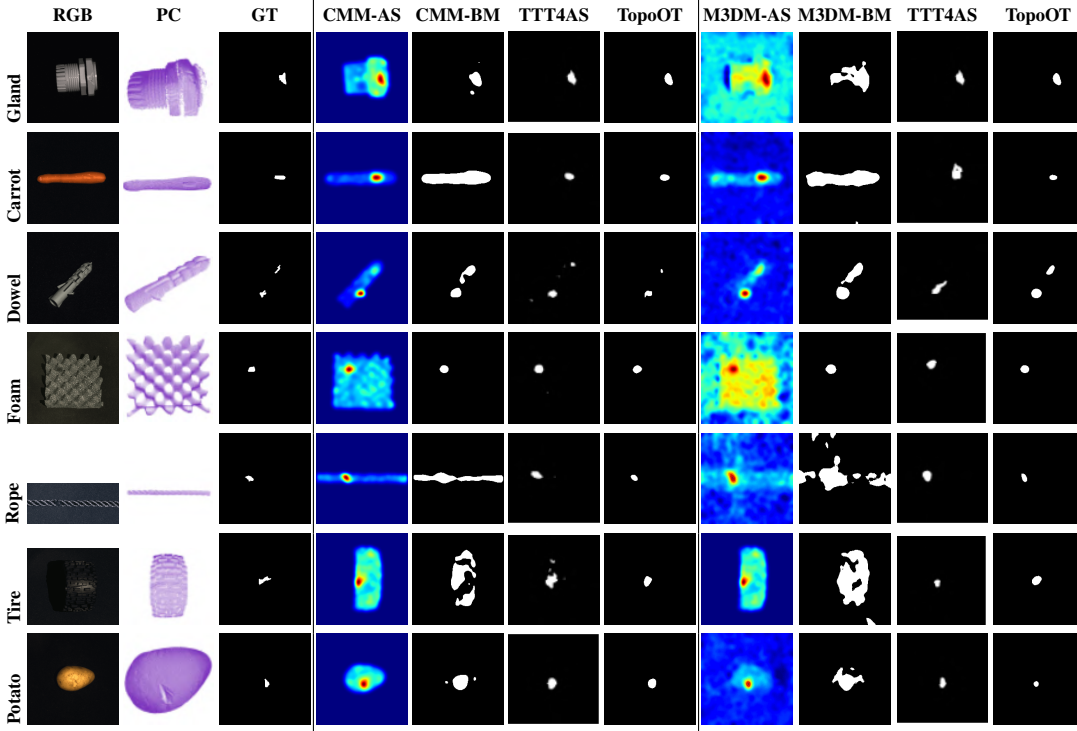


Figure 4. Qualitative comparison of AD&S methods for different objects using on 3D MvTec AD Dataset.

implementation.

Figure 4 presents qualitative comparisons for the M3DM and CMM backbones across all binarization baselines. The visualizations demonstrate that TopoOT consistently yields the most accurate segmentations. While THR exhibits severe over-segmentation and TTT4AS produces fragmented results, TopoOT effectively filters noise and maintains high topological fidelity. These visual improvements align with the ground truth and confirm the robustness of our framework in localized 3D anomaly detection.

A.6. Optimal Transport Preliminaries

For completeness, we recall the Optimal Transport (OT) formulations underlying Eq. (2). Let $P = \{p_i, w_i\}_{i=1}^m$ and $Q = \{q_j, v_j\}_{j=1}^n$ be two discrete probability measures with weights $w \in \Delta^m$, $v \in \Delta^n$, and cost matrix $C(i, j) = \|p_i - q_j\|_2^2$. The classical 2-Wasserstein distance is defined as

$$W_2^2(P, Q) = \min_{\Pi \in \mathcal{U}(w, v)} \langle C, \Pi \rangle,$$

where $\Pi \in \mathbb{R}_+^{m \times n}$ is a transport plan and $\mathcal{U}(w, v) = \{\Pi \mid \Pi \mathbf{1} = w, \Pi^\top \mathbf{1} = v\}$ denotes the set of admissible couplings. While exact OT provides a principled alignment, solving this linear program has $O(m^3 \log m)$ complexity, and the resulting optimal plans are typically sparse. In practice, sparsity can make OT couplings numerically sensitive, that is, small perturbations in the support points may lead to abrupt changes in the optimal plan (Peyré et al., 2019).

To improve robustness and computational efficiency, we adopt the *entropy-regularised* variant, known as the Sinkhorn distance (Cuturi, 2013; Peyré et al., 2019):

$$W_\varepsilon(P, Q) = \min_{\Pi \in \mathcal{U}(w, v)} \langle C, \Pi \rangle + \varepsilon H(\Pi),$$

where $H(\Pi) = \sum_{i,j} \Pi(i, j)(\log \Pi(i, j) - 1)$ is the negative entropy of Π . The regularisation parameter $\varepsilon > 0$ controls smoothness: large ε yields dense couplings, while small ε approaches the exact Wasserstein distance.

In our pipeline, persistence diagrams are constructed using GUDHI (cubical complexes), but all transport computations are carried out with POT’s `ot.sinkhorn(..., reg=ε)` routine¹. Thus, the couplings Π^* appearing in Sec. 3.2 and Appendix A.7 are entropy-regularised OT plans. This choice ensures numerical stability, differentiability, and Lipschitz continuity, which underlie the stability and generalisation guarantees established in Appendix A.7.

A.7. Conceptual Motivation

A central motivation of our framework is that anomaly segmentation under distribution shift can be interpreted through the discrepancy between distributions of persistence features. Let \mathcal{D}_{sub} and \mathcal{D}_{sup} denote the empirical distributions of birth–death components extracted from the sub- and super-level filtrations (Sec. 3.1). The entropic OT distance

$$W_\varepsilon(\mathcal{D}_{\text{sub}}, \mathcal{D}_{\text{sup}}) = \min_{\Pi \in \mathcal{U}(\mathcal{D}_{\text{sub}}, \mathcal{D}_{\text{sup}})} \langle C, \Pi \rangle + \varepsilon H(\Pi)$$

quantifies the minimal cost of aligning structural information across the two filtrations. Computing W_ε identifies components with stable, low-cost couplings, from which OT-guided pseudo-labels \tilde{Y}_{OT} are derived (Sec. 3.2).

By combining the classical stability of persistence diagrams with the smooth dependence of entropic OT on point locations, this construction is expected to yield pseudo-labels that are more stable under small local perturbations of the anomaly map.

Beyond stability, this perspective connects conceptually to classical discrepancy-based domain adaptation (DA). In the DA setting (Redko et al., 2017), the target risk can be upper bounded by a source risk plus a discrepancy term (e.g., a Wasserstein distance). We use this framework purely as an analogy: in our setting, the “source” and “target” distributions correspond to persistence features extracted at different filtration levels or under distribution shift. We do not train hypotheses within the OT step, nor do we claim a new DA bound; the analogy simply clarifies why reducing OT discrepancy across filtrations correlates with empirical robustness.

¹<https://pythonot.github.io/>

Setup. Let P_k^f denote the persistence diagram extracted from the $f \in \{\text{sub}, \text{sup}\}$ filtration at threshold τ_k . We compute entropic OT distances between augmented diagrams (Sec. A.6), allowing each point $p = (b, d)$ to match either a point in another diagram or its diagonal projection. Let $\Pi_{k \rightarrow \ell}^*$ be the optimal transport plan between P_k^f and P_ℓ^g with ground cost $C(i, j) = \|p_i - q_j\|_2^2$. The cross-level stability score $s(c)$ for a feature c is defined in Sec. 3.2.

Observation: Stability under perturbations. Persistence diagrams are stable under perturbations of the underlying function, in the sense that moving each point by at most ρ perturbs the diagram by at most $O(\rho)$ in standard diagram distances. Entropically regularised OT inherits this smooth dependence on point positions. Consequently, the chained stability scores used for feature selection vary smoothly under ρ -bounded perturbations. Features separated by a sufficiently large margin retain their relative ranking.

Observation: Behaviour of entropic OT along chains. The entropic OT W_ε debiased counterpart, the Sinkhorn divergence S_ε , is a true metric and obeys a triangle inequality (Feydy et al., 2019). This provides a useful analogy for interpreting chained OT behaviour, if pairwise discrepancies along a filtration chain decrease, the corresponding Sinkhorn divergence between the endpoints also decreases. Although our method operates directly on W_ε , we observe empirically that reducing local OT costs across levels suppresses spurious cross-level inconsistencies, consistent with the behaviour suggested by the metric structure of S_ε .

Interpretation. Together, the stability of persistence diagrams and the behaviour of entropic OT provide intuition for why the OT-chaining mechanism is robust and why it can reduce cross-level discrepancy in practice. These results are conceptual and do not constitute a new formal theory; they serve to situate the empirical behaviour observed in our experiments within existing stability principles from topological data analysis and discrepancy-based generalisation theory.

A.8. Cubical Persistence

A *primitive interval* is $J = [k, k + 1] \subset \mathbb{R}$ with $k \in \mathbb{Z}$, called a 1-cube, the degenerate case $[k]$ is a 0-cube. A d -dimensional *elementary cube* is the Cartesian product

$$CU = J_1 \times \cdots \times J_d \in \mathbb{R}^d, \quad (6)$$

e.g., vertices, edges, squares, and voxels in 3D.

The boundary of CU is

$$\partial CU = \sum_{i=1}^d (-1)^{i+1} (J_1 \times \cdots \times \partial J_i \times \cdots \times J_d), \quad (7)$$

where $\partial J_i = \{k, k + 1\}$. A cube CU is a *subcube* of CU' if $J_i \subseteq J'_i$ for all i .

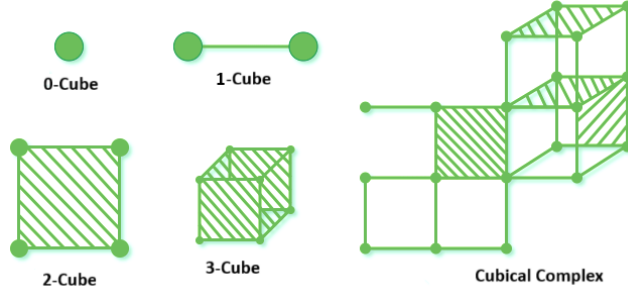


Figure 5. Elementary cubes of different dimensions and an example cubical complex.

A *cubical complex* \mathcal{K} is a set of cubes closed under subcubes and boundaries, ensuring structural coherence across dimensions (Fig. 5).

The chain group $CU_n(K)$ is the free Abelian group on n -cubes, linked by boundary maps

$$\cdots \rightarrow CU_{n+1}(K) \xrightarrow{\partial_{n+1}} CU_n(K) \xrightarrow{\partial_n} CU_{n-1}(K) \rightarrow \cdots,$$

with $\partial_n \circ \partial_{n+1} = 0$. Cycles and boundaries are

$$Z_n(K) = \ker(\partial_n), \quad B_n(K) = \text{im}(\partial_{n+1}),$$

and the n -th homology group is $H_n(K) = Z_n(K)/B_n(K)$.

A *filtration function* $f_K : K \rightarrow \mathbb{R}$ activates cubes monotonically: $P \sqsubseteq Q \Rightarrow f_K(P) \leq f_K(Q)$. This defines sublevel and superlevel sets:

$$K(a_i) = f_K^{-1}((-\infty, a_i]), \quad K^\uparrow(b_i) = f_K^{-1}([b_i, +\infty)). \quad (8)$$

Filtrations induce homology maps

$$H_k(K_0) \xrightarrow{\varphi_{01}} H_k(K_1) \xrightarrow{\varphi_{12}} \dots \xrightarrow{\varphi_{n-1,n}} H_k(K_n),$$

forming the persistence module

$$\mathcal{P} = \{H_k(K_i), \varphi_{ij}\}_{0 \leq i \leq j \leq n}.$$

Each topological feature σ has birth b_σ , death d_σ , and persistence $d_\sigma - b_\sigma$. The collection of intervals $[b_\sigma, d_\sigma)$ forms the *barcode*, while the *persistence diagram* (PD) encodes these as birth–death points in \mathbb{R}^2 . To integrate with ML models, PDs are vectorised via

$$\Phi : \text{PD} \rightarrow \mathbb{R}^M.$$

A.9. Ablation Study on Top-K Components

We performed a dedicated sensitivity analysis of the Top-K selection. As shown in the Table 23, we evaluate $K \in 1, 2, 3, 4, 5$ across datasets and backbones. We find that a fixed value of $K=1$ yields the most stable and highest F1-scores (PatchCore: 0.522; CMM: 0.482; M3DM: 0.490). As K increases, F1 consistently decreases, even though recall rises. This trend is expected; the highest-ranked components are those with the strongest OT-stability and largest persistence, whereas lower-ranked components correspond to short-persistence, less reliable structures. Including these additional components introduces noise into the pseudo-labels and degrades precision, leading to lower F1. Since $K=1$ is the most robust choice across datasets and architectures, we fix it globally in all experiments.

Table 23. Effect of retaining the Top- K OT-stable components on anomaly segmentation. Each row corresponds to keeping the K highest-ranked components (ranked by OT-stability and persistence).

| Top- K Components Retained | 2D-PatchCore | | | 3D-CMM | | | 3D-M3DM | | |
|------------------------------|--------------|--------------|--------------|--------------|--------------|--------------|--------------|--------------|--------------|
| | Precision | Recall | F1 | Precision | Recall | F1 | Precision | Recall | F1 |
| K = 1 | 0.550 | 0.720 | 0.522 | 0.427 | 0.845 | 0.482 | 0.564 | 0.767 | 0.490 |
| K = 2 | 0.462 | 0.818 | 0.474 | 0.411 | 0.753 | 0.410 | 0.323 | 0.809 | 0.434 |
| K = 3 | 0.405 | 0.829 | 0.431 | 0.392 | 0.671 | 0.403 | 0.286 | 0.950 | 0.356 |
| K = 4 | 0.358 | 0.901 | 0.415 | 0.381 | 0.666 | 0.397 | 0.177 | 0.961 | 0.334 |
| K = 5 | 0.325 | 0.911 | 0.380 | 0.354 | 0.576 | 0.388 | 0.121 | 0.966 | 0.199 |

A.10. Qualitative Analysis on Textural Anomaly Cases

Figure 6 presents hard texture categories such as carpet, grid, and wood where the backbone anomaly maps are diffuse and provide weak topological contrast, so the sublevel and superlevel filtrations split into many small components that only partially overlap the ground truth and can add small islands in normal regions. Cross filtration OT alignment reduces fragmentation and concentrates the support, which usually makes the final TopoOT masks cleaner and closer to the ground truth than TTT4AS, but subtle defects can still be under segmented and minor false positives may remain. These cases clarify the main constraint that TopoOT cannot recover structure that is not present in the backbone scores, and fully unsupervised test time training provides no explicit shape prior to correct fine texture errors, which motivates stronger filtration signals through multi scale smoothing or local texture statistics combined with anomaly scores and additional regularisation that discourages isolated or overly fragmented pseudo labels.

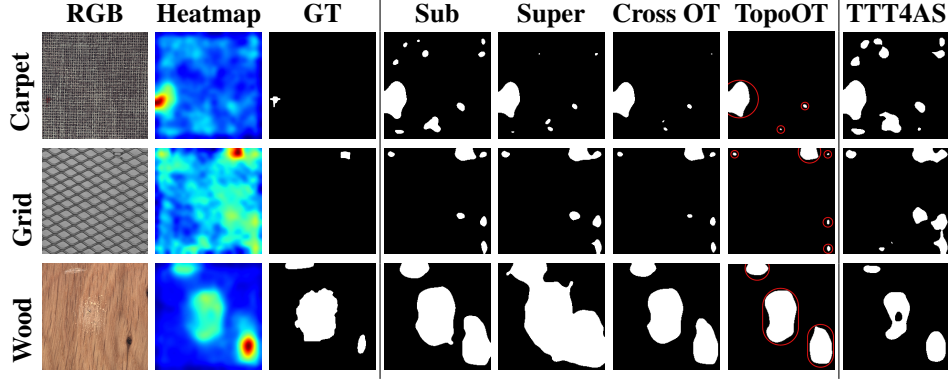


Figure 6. Qualitative examples on texture-heavy categories (carpet, grid, wood). From left to right: RGB image, backbone anomaly heatmap, ground truth (GT), binary masks from sublevel and superlevel filtrations, OT-guided pseudo-label (Cross OT), final TopoOT prediction, and TTT4AS. TopoOT reduces spurious fragments and sharpens the region compared to TTT4AS, but residual under-segmentation and small false positives remain, illustrating the challenges posed by weak topological signal in purely textural anomalies.

A.11. Detailed TopoOT Algorithm

Algorithm 1 TopoOT: Topology-Aware Optimal Transport for Anomaly Segmentation

Input : Test image x ; Frozen Backbone $F(\cdot)$; Thresholds $\mathcal{T} = \{\tau_1 < \dots < \tau_N\}$; OT Reg. ε ; Weights α, λ, m ; Top- K .
Output : Binary Segmentation Mask \hat{Y}^{bin}

Extract backbone features $Z = F(x)$ and scalar anomaly map $A(x) \in [0, 1]^{H \times W}$

/* **Multi-Scale Filtering** (Sec. 3.1) */

foreach filtration type $f \in \{\text{sub}, \text{sup}\}$ **do**

- Initialize empty diagram list $\mathcal{D}_f \leftarrow []$ **foreach** threshold $\tau_k \in \mathcal{T}$ **do**
- Construct cubical complex $K_{\tau_k}^f$ on the level set $S_{\tau_k}^f$ (as defined in Sec.3.1) Compute persistence diagrams $P_h^f[\tau_k] = \text{PH}_h(K_{\tau_k}^f)$
- for $h \in \{0, 1\}$ Append $\{P_h^f[\tau_k]\}_{h \in \{0, 1\}}$ to \mathcal{D}_f

/* **Stability Scoring** (Sec. 3.2) */

foreach $f \in \{\text{sub}, \text{sup}\}$ **do**

- Initialize feature chains \mathcal{C}_f from \mathcal{D}_f **foreach** sequential pair (P_k, P_{k+1}) in \mathcal{D}_f **do**
- Compute Cost Matrix C ; Solve Entropic OT Π_{intra}^* ; // Eq. 1
- foreach** feature c in chain **do**
- $s_{\text{intra}}(c) \leftarrow \max_j \left(\frac{\Pi_{\text{intra}}^*(i(c), j)}{1 + \sqrt{C(i(c), j)}} \right) \cdot \alpha \cdot \text{pers}(c)$; // Eq. 2

 Filter \mathcal{C}_f : Retain chains with high cumulative s_{intra}

Compute OT plan Π_{cross}^* between surviving sets \mathcal{C}_{sub} and \mathcal{C}_{sup} **foreach** candidate $c \in \mathcal{C}_{\text{sub}} \cup \mathcal{C}_{\text{sup}}$ **do**

- $s_{\text{cross}}(c) \leftarrow \max_j \left(\frac{\Pi_{\text{cross}}^*(i(c), j)}{1 + \sqrt{C(i(c), j)}} \right) \cdot \alpha \cdot \text{pers}(c)$

$\mathcal{C}^* \leftarrow$ Select Top- K ranked candidates based on $s_{\text{cross}}(c)$; // See Ablation A.10

/* **Backprojection to Pixel Space** (Sec. 3.2) */

Initialize pseudo-label mask $\tilde{Y}_{\text{OT}} \leftarrow 0$ on Ω **foreach** candidate $c \in \mathcal{C}^*$ **do**

- Retrieve death time d_c of c from its persistence diagram Set backprojection threshold $\tau_{\text{bp}}(c) \leftarrow d_c$ Define pixel support $\Gamma(c) \leftarrow \{p \in \Omega : A(p) \geq \tau_{\text{bp}}(c)\}$ Update mask $\tilde{Y}_{\text{OT}}(p) \leftarrow \tilde{Y}_{\text{OT}}(p) \vee \mathbf{1}_{\Gamma(c)}(p)$ for all p

/* **TopoOT Test-Time Training** (Sec. 3.3) */

Initialize lightweight head h_{ψ} (MLP) **while** not converged **do**

- Forward: $\hat{Y}_{\text{logits}} = h_{\psi}(Z)$, $\hat{Y}_{\text{prob}} = \sigma(\hat{Y}_{\text{logits}})$, $z_p = \text{Normalize}(\hat{Y}_{\text{logits}}[p])$
- $\mathcal{L}_{\text{OT}} = \|\hat{Y}_{\text{prob}} - \tilde{Y}_{\text{OT}}\|_2$
- Sample pixel pairs (p, q) based on \tilde{Y}_{OT} (Same/Diff class) $\mathcal{L}_{\text{con}} = (1 - y_{pq})\|z_p - z_q\|_2^2 + y_{pq}[\max(0, m - \|z_p - z_q\|_2)]^2$; // Eq. 3
- Update $\psi \leftarrow \psi - \eta \nabla_{\psi} (\mathcal{L}_{\text{OT}} + \lambda \mathcal{L}_{\text{con}})$

/* **Inference** */

return $\hat{Y}^{\text{bin}} \leftarrow \text{AdaptiveDecisionRule}(h_{\psi}(Z))$
